

Acoustic- and elastic-waveform inversion with total generalized p-variation regularization

Kai Gao^{*,1} and Lianjie Huang¹

¹Los Alamos National Laboratory, Geophysics Group, MS D452, Los Alamos,
NM 87545, USA

Abstract

Geophysical models usually contain both sharp interfaces and smooth variations, and it is difficult to accurately account for both of these two types of medium parameter variations using conventional full-waveform inversion methods. In addition, sparse geometry, noisy data and source encoding usually lead to strong inversion artifacts. We develop a novel full-waveform inversion method for acoustic and elastic waves using a total generalized p-variation regularization scheme to address these challenging problems. We decompose the full-waveform inversion into two subproblems and solve these two minimization subproblems using an alternating-direction minimization strategy. One important advantage of the total generalized p-variation regularization scheme is that it can simultaneously reconstruct sharp interfaces and smooth background variations of geophysical parameters. Such capability can also effectively suppress the noises in source-encoded inversion and sparse-data inversion, or inversion of noisy data. We demonstrate the advantages of our new full-waveform inversion algorithm using a checkerboard model, a modified elastic SEG/EAGE overthrust model, and a land field seismic dataset. Our results of synthetic and field seismic data demonstrate that our new method reconstructs both smooth background variations and sharp interfaces of subsurface geophysical properties accurately, reduces the inversion artifacts caused by source encoding, noisy data

*Corresponding Author; kaigao87@gmail.com (K. Gao); ljh@lanl.gov (L. Huang)

or insufficient data coverage effectively, and provides a useful tool for accurate and reliable inversion of field seismic data.

1 Introduction

Full-waveform inversion (FWI) attempts to reconstruct subsurface medium properties by iteratively minimizing the difference between synthetic and observed data (Tarantola, 1984, 1986; Mora, 1987, 1988). As self-explained by its name, FWI uses full wavefield information, including both the amplitude and the traveltimes of seismic signals, to invert for subsurface medium properties.

Theoretically, FWI should be the most accurate inversion method for subsurface model building. However, numerous studies have shown that FWI is a highly nonlinear, ill-posed inverse problem (e.g., Luo and Schuster, 1991; Virieux and Operto, 2009). The misfit function of FWI may have numerous local minima. This characteristic of FWI usually leads to unsuccessful inversions and unreliable results when the initial model used in FWI is far away from the true model. This problem is often true in practical applications, particularly when the subsurface geology is complicated and/or the acquired seismic data are sparse and noisy.

Given the difficulties in applying the conventional FWI to practical problems, numerous studies have been conducted to seek a practically applicable and reliable inversion scheme, and continuous efforts are one of the most active research areas in the geophysical community. These studies are mostly in three categories.

The first category is employing a more convex function as the misfit function of FWI, rather than using the traditional ℓ_2 -norm waveform difference. The misfit function in the conventional FWI relies on the absolute waveform matching between synthetic data and observed data, and cycle skipping issue can easily occur if there is a significant phase and/or amplitude difference. Studies of seeking more convex function include the wave-equation traveltimes based misfit function (Luo and Schuster, 1991; Luo et al., 2016), the envelope-based misfit function (Wu et al., 2014; Chi et al., 2014), the instantaneous-phase-based misfit function (Bozdağ et al., 2011; Jiao et al., 2015), the correlation-based misfit function (Van Leeuwen and Mulder, 2010; Luo and Sava, 2011; Chi et al., 2015; Choi and Alkhalifah, 2016), the deconvolution-based misfit function (Luo and Sava,

2011; Warner and Guasch, 2016), the dynamic-time-warping-based misfit function (Ma and Hale, 2013), the Huber-norm misfit function (Guitton and Symes, 2003; Ha et al., 2009), and the optimal transport approach (Métivier et al., 2016a,b; Yang et al., 2017, 2018), etc. These misfit functions are generally more convex with respect to model perturbations, and therefore less prone to the cycle skipping issue.

The second category is conducting FWI in a Gauss-Newton or quasi-Newton minimization framework. Conventional FWIs are essentially based on the first-order perturbation theory. The second-order terms (or equivalently the Hessian) can be important in FWI to obtain accurate and high-resolution model estimations (Pratt et al., 1998; Tang and Lee, 2010; Fichtner and Trampert, 2011). The Hessian can also be important in multi-parameter inversion (Pan et al., 2016). A direct computation of the inverse Hessian can be prohibitively expensive using current computational architecture (Fichtner and Trampert, 2011), and therefore several approximation methods were developed, including the limited-memory BFGS (L-BFGS) scheme (e.g., Nocedal and Wright, 2006), the truncated Newton method (Métivier et al., 2013, 2017), the quasi-Newton method with projected Hessian (Ma and Hale, 2013), combined Newton and conjugate gradient schemes (Epanomeritakis et al., 2008), and pseudo-Gauss-Newton scheme (Pan et al., 2015), etc. Several preconditioners were also developed to approximate the Hessian (e.g., Zhang et al., 2012).

The third category is employing regularization to accelerate the convergence. Applying regularization to geophysical inverse problems has a fairly long history (Zhdanov, 2002), and the Tikhonov regularization is probably the most frequently used regularization scheme (Tikhonov et al., 1995; Asnaashari et al., 2013).

The Tikhonov regularization tends to produce smooth models. In image analysis and processing, the total variation (TV) method (Rudin et al., 1992) was developed to promote sharp interfaces in the image. The method has been applied in geophysical inverse problems to promote the sharp interfaces of layers (Anagaw, 2011). Guitton (2012) designed a blocky regularization scheme for FWI. He employed a ℓ_1 -norm and a Cauchy function to enforce blockiness of the model. The blocky regularization is essentially edge-promoting: it can enforce sharp interfaces even at locations where interfaces probably do not exist, a feature in accordance with minimizing the total variation of a model. Therefore, the inversion results tend to be piecewise constant. This feature is also an inherent limitation of the first-order TV regularization.

The first-order TV regularization can be less efficient when the data is noisy or the model is complex. [Lin and Huang \(2014\)](#) developed a novel regularized FWI based on a modified TV (MTV) regularization scheme. They decomposed FWI into two interlacing inversion problems: one is the conventional FWI with a Tikhonov regularization term, and the other is an image denoising problem using the first-order TV method. The second problem is solved efficiently with the split-Bregman iteration, a technique that is proven to be especially suitable to produce clean and accurate TV denoising results ([Goldstein and Osher, 2009](#)). The model parameter and the auxiliary model parameter are updated in an alternating-direction approach, resulting in an efficient first-order TV regularized FWI. However, this regularization scheme is based on the first-order TV. Although it avoids spike noises and provides more reliable inversion results, it still cannot avoid the inherent disadvantage of the first-order TV, i.e., the staircase artifacts in inversion results.

[Esser et al. \(2016\)](#) developed an asymmetric TV regularized FWI. The asymmetric TV, or hinge-loss constraint TV as they called, penalizes the model discontinuities only in the vertical direction. They show that this asymmetric TV regularized FWI can facilitate the automatic delineation of high-contrast medium parameter anomalies such as salt bodies, as well as depth structures.

The Tikhonov and TV regularizations are not the only regularization schemes used in full-waveform inversion. [Guitton et al. \(2012\)](#) developed a preconditioned FWI using the geological information derived from the migration image. The preconditioner is solved via estimating the local dip information from the migration image followed by a directional Laplacian filter ([Hale, 2007](#)). [Lewis et al. \(2014\)](#) developed a similar approach based on the anisotropic diffusion filtering, where the structural tensor is estimated from a migration image. In their approach, the gradient is preconditioned based on the geological structures derived from structural images, thus becomes geologically meaningful. In the case of sparse sources and therefore insufficient subsurface model coverage, such preconditioning can facilitate faster convergence towards meaningful inversion results. [Xue et al. \(2017\)](#) developed a similar regularization scheme using sparsity promotion in the seislet domain.

The total generalized variation ([Bredies et al., 2010](#); [Knoll et al., 2011](#); [Zhang et al., 2016](#)) is a technique that incorporates the higher-order total variations in image reconstruction. It is usually applied to various problems in its second-order form with a ℓ_1 -norm framework. The total

generalized variation can reconstruct both the sharp interfaces and smooth variations of an image, leading to fewer artifacts compared with the first-order total-variation approach.

In medical imaging, the ℓ_p -norm ($0 < p < 1$) compressive-sensing (Chartrand, 2009; Chartrand et al., 2013) is surprisingly effective to reconstruct images using extremely sparse measurements compared with the ℓ_1 -norm compressive sensing techniques (Candes et al., 2006; Donoho, 2006; Candes and Wakin, 2008; Goldstein and Osher, 2009).

We develop a novel full-waveform inversion method for acoustic and elastic waves using a total generalized p -variation regularization scheme (TGPV-FWI). We combine the advantages of ℓ_p -norm compressive sensing techniques and the second-order total variation to reconstruct both sharp interfaces and smooth background variations of geophysical parameters. We formulate our TGPV-FWI in an alternating-direction minimization framework. We decompose the TGPV-FWI into two interlacing minimization problems. The first minimization problem is a conventional FWI problem with the Tikhonov regularization, whereas the second minimization problem is a second-order compressive sensing model denoising problem. Once the second subproblem is solved correctly, we only need to add the difference between the FWI model in the last inversion and its “denoising” result from the second minimization problem to the gradient in the current inversion step. This strategy forces the inversion to evolve towards the TGPV model that is less prone to artifacts when seismic data are sparse, noisy or when using dynamic source encoding. With this alternating minimization framework, the FWI eventually converges to a more accurate and reliable result.

Our paper is organized as follows. In the Methodology section, we present the formulation of our new TGPV-FWI. We present the detailed algorithms for solving the second subproblem and our new TGPV-FWI in two appendices. In the Numerical Results section, we give three numerical examples, including two synthetic data examples and one field data example, to verify the advantages of our new TGPV-FWI over FWI with the conventional regularization schemes including the Tikhonov and TV regularizations. We give our findings in the Conclusions section.

2 Methodology

We formulate our new full-waveform inversion with the total generalized p-variation regularization (TGPV-FWI) as the following minimization problem:

$$\mathbf{m}^* = \arg \min_{\mathbf{m}} \left\{ \frac{1}{2} \|\mathbf{d} - f(\mathbf{m})\|_2^2 + \lambda \mathcal{T}_p(\mathbf{m}) \right\}, \quad (1)$$

where \mathbf{d} is an observed dataset, $f(\mathbf{m})$ is a synthetic dataset, \mathbf{m} is the medium parameter model to be inverted, and $\mathcal{T}_p(\mathbf{m})$ is the TGPV regularization term.

Unlike the conventional regularization schemes such as the Tikhonov and TV regularizations that are defined using the ℓ_2 -norm and ℓ_1 -norm, respectively, the TGPV regularization term $\mathcal{T}_p(\mathbf{m})$ is defined through a ℓ_p -norm minimization problem:

$$\mathcal{T}_p(\mathbf{m}) = \arg \min_{\mathbf{w}} \left\{ \alpha_0 \|\nabla \mathbf{m} - \mathbf{w}\|_p^p + \alpha_1 \|\varepsilon(\mathbf{w})\|_p^p \right\}, \quad (0 < p < 1) \quad (2)$$

where $\mathbf{w} = (\mathbf{w}_x, \mathbf{w}_y)$ is an auxiliary vector variable. The ℓ_p -norm (or more precisely, the ℓ_p quasi-norm) with $0 < p < 1$ of a number $\mathbf{x} \in \mathbb{R}^n$ is defined as

$$\|\mathbf{x}\|_p = \left(\sum_{i=1}^n |x_i|^p \right)^{1/p}. \quad (3)$$

In the 2D case, the gradient of model \mathbf{m} is

$$\nabla \mathbf{m} = \begin{bmatrix} \nabla_x \mathbf{m} \\ \nabla_y \mathbf{m} \end{bmatrix}, \quad (4)$$

and the symmetric gradient $\varepsilon(\cdot)$ reads

$$\varepsilon(\mathbf{w}) = \begin{bmatrix} \nabla_x \mathbf{w}_x & \frac{1}{2}(\nabla_x \mathbf{w}_y + \nabla_y \mathbf{w}_x) \\ \frac{1}{2}(\nabla_x \mathbf{w}_y + \nabla_y \mathbf{w}_x) & \nabla_y \mathbf{w}_y \end{bmatrix}. \quad (5)$$

The minimization problem defining the TGPV regularization term is based on the total generalized variation in image processing (Bredies et al., 2010; Knoll et al., 2011; Zhang et al., 2016). The advantage of the total generalized variation is that it penalizes both the first-order gradient and high-order gradients of an image or a model, and thus it can effectively avoid the staircase effect compared with the first-order total variation. The advantage of the ℓ_p -norm penalty over the traditional ℓ_1 -norm penalty is observed from the results in compressive-sensing medical imaging

(Chartrand, 2009), in which it can handle even sparse data than the ℓ_1 -norm for accurate image reconstruction. The ℓ_p -norm regularization term leads to a nonconvex minimization problem. This introduces difficulties in solving the FWI problem. In the context of compressive sensing, Chartrand (2009) shows that there exist techniques to efficiently solve the ℓ_p -norm nonconvex problem. We solve our TGPV-FWI using the similar approaches.

Unlike the conventional TV-regularized FWI, it is impossible to solve the minimization problem in eq. (1) directly. To solve our TGPV-FWI efficiently, we reformulate the minimization in eq. (1) into an alternating-direction minimization problem as by Lin and Huang (2014):

$$\{\mathbf{m}^*, \mathbf{u}^*\} = \arg \min_{\mathbf{m}, \mathbf{u}} \left\{ \frac{1}{2} \|\mathbf{d} - f(\mathbf{m})\|_2^2 + \lambda_1 \|\mathbf{m} - \mathbf{u}\|_2^2 + \lambda_2 \mathcal{F}_p(\mathbf{u}) \right\}, \quad (6)$$

which can be decomposed into two interlacing minimization problems:

$$\mathbf{m}^{(l+1)} = \arg \min_{\mathbf{m}} \left\{ \frac{1}{2} \|\mathbf{d} - f(\mathbf{m})\|_2^2 + \lambda_1 \|\mathbf{m} - \mathbf{u}^{(l)}\|_2^2 \right\}, \quad (7a)$$

$$\mathbf{u}^{(l+1)} = \arg \min_{\mathbf{u}} \left\{ \frac{1}{2} \|\mathbf{m}^{(l+1)} - \mathbf{u}\|_2^2 + \lambda_2 \mathcal{F}_p(\mathbf{u}) \right\}, \quad (7b)$$

where l is the iteration number in the FWI. That is, the medium parameter \mathbf{m} and the auxiliary variable \mathbf{u} are updated alternatively in the inversion procedure. The auxiliary variable serves as the prior information in the TGPV-FWI, and it is also updated through iterations.

The first minimization problem in eq. (7a) is a conventional FWI problem with a zeroth-order Tikhonov regularization term. Numerous methods can be adopted to solve this nonlinear minimization problem, such as the conjugate-gradient (CG) method and the limited-memory BFGS (L-BFGS) method (Nocedal and Wright, 2006), etc. Misfit functions other than the simple ℓ_2 -norm-squared waveform difference in eq. (1), as discussed in the Introduction, can also be applied to the first subproblem. We adopt the split-Bregman iteration methodology (Goldstein and Osher, 2009) to solve the second minimization problem.

We show detailed algorithms for solving the second minimization problem in the 2D and 3D cases in Appendices A and B, respectively.

Our TGPV-FWI contains several parameters to be adjusted. We describe how to select these parameters in the following.

The positive parameter λ_1 controls the “strength” of the regularization term in the first minimization problem, and a larger λ_1 leads to a stronger TGPV regularization. In applications, we use

the following simple rule to determine λ_1 :

$$\lambda_1(\mathbf{m}) = \gamma \frac{\|\nabla\chi(\mathbf{m})\|_2}{\|\mathbf{m} - \mathbf{u}\|_2}, \quad (8)$$

where γ is a scaling factor that can be tuned during iterations, and $\nabla\chi(\mathbf{m})$ represents the gradient of the misfit function w.r.t. some model parameter at certain iteration. $\|\cdot\|_2$ represents the ℓ_2 -norm of a quantity. For different applications, the value of γ can vary. Normally, a value between 0.05 to 0.5 should be suitable for most applications, and larger values of γ are not encouraged. In our numerical tests, we determine different λ_1 s for different model parameters (e.g., V_p or V_s in elastic-waveform inversion) in each iteration using eq. (8). We find $\gamma = 0.1$ can serve as a suitable value.

The method to determine the regularization parameter λ_1 is slightly different from that in such as [Lin and Huang \(2014\)](#). The general principle, however, is in common: the regularization term and the data misfit term should be in decent balance to avoid excessive or insufficient regularization.

There are six parameters in the second minimization problem in eq. (A-11): α_0 , α_1 , η_0 , η_1 , μ and the norm p . The positive parameter λ_2 (or equivalently $1/\mu$) controls the “strength” of denoising in the second minimization problem, and a larger λ_2 (or equivalently a smaller μ) leads to a stronger smoothing. Note that the smoothing is not a spatial smoothing in a usual sense, such as that of Gaussian spatial filtering; it is a smoothing in the total-variation sense. In extreme cases, $\mu \rightarrow 0$ can smooth out all the features of a model, while $\mu \rightarrow +\infty$ leaves the model unchanged. The most important feature of this smoothing is that it simultaneously preserves sharp interfaces and smooth variations of the model in the framework of the high-order total variation.

For the other five parameters, our extensive tests show that for most of, if not all, practical applications, $p = 0.5$, $\alpha_0 = 1$, $\alpha_1 = 1$ or 2 , and $\eta_0 = 2\mu$ and $\eta_1 = \frac{\alpha_1}{\alpha_0}\eta_0$ can solve the second subproblem to produce fairly accurate results.

Therefore, for the second subproblem, only the parameter μ should be tuned for different FWI problems. This indicates that in our TGPV-FWI, in most cases we only need to tune two parameters, the Tikhonov regularization coefficient λ_1 and the regularization parameter μ (or equivalently λ_2) as described above, leading to an efficient inversion system.

We summarize our TGPV-FWI algorithm in Appendix C.

3 Numerical Results

In the following, we use Tikhonov-TV to denote the FWI with the Tikhonov regularization, TV-FWI to denote the FWI with the TV regularization, and TGPV-FWI to denote the FWI with our TGPV regularization.

3.1 Synthetic data example I: Checkerboard model

Our TGPV-FWI for acoustic and elastic waves can be used for either large-scale tomography of the Earth using earthquake data or small-scale seismic reflection inversion. For the former case, transmission seismic waves are mostly used. To verify the improved inversion accuracy of our new TGPV-FWI algorithm using mostly transmission signals, we design a checkerboard model with randomly distributed sources within the model. The goal of this numerical test is to verify the applicability of our new method using mostly transmission signals, rather than using Earthquake data.

The model is defined in a region of 970 m \times 970 m with a grid interval of 10 m in both directions. This checkerboard model is composed of a smoothly-varying background and checkerboard velocity perturbations, as shown in Fig. 1a. The velocity perturbation is approximately 10 percent throughout the model, and the perturbation can be as high as approximately 20 percent in some regions. We use a smooth velocity model without the large-contrast velocity perturbations as displayed in Fig. 1b as the initial velocity model for FWI.

We place a total of 24 sources randomly distributed throughout the model (black stars in Fig. 1b) and a total of 356 receivers near the boundaries of the model (blue triangles in Fig. 1b).

The source wavelet is a Ricker wavelet with a center frequency of 20 Hz. We employ the L-BFGS inversion framework and terminate the inversion after 150 iterations. We conduct three tests using the Tikhonov-FWI, TV-FWI and TGPV-FWI.

Figs. 2a, b and c show the FWI inversion results obtained using the Tikhonov-FWI, TV-FWI and TGPV-FWI, respectively. The Tikhonov-FWI produces a smooth checkerboard inversion result with missing sharp interfaces of checkerboard blocks. The TV-FWI preserves the sharp interfaces of the checkerboard blocks, yet within the blocks, the inversion result shows clear the piecewise-constant feature, or more commonly, the staircase effect. Our TGPV-FWI accurately

reconstructs not only the sharp block interfaces, but also the smooth variations inside the blocks.

To quantitatively compare the inversion results in Fig. 2, we plot velocity profiles at the position of $X = 500$ m from the three inversion results, and show them in Figs. 3a, b and c for Figs. 2a, b and c, respectively. This comparison further demonstrates the superior capability of our TGPV-FWI in reconstructing both the sharp interfaces and smooth variations in the checkerboard model.

Fig. 4 shows that the our TGPV-FWI results in smallest data and model misfits among the three FWI methods used, demonstrating the improved inversion accuracy of our TGPV-FWI.

3.2 Synthetic data example II: Modified elastic SEG/EAGE overthrust model

We use a modified elastic SEG/EAGE overthrust model to verify the efficacy of our TGPV-FWI method for elastic-waveform inversion using surface reflection data. In the following numerical tests, we verify our TGPV-FWI method for: (1) noise-free data with adequate numbers of sources and receivers (a regular source/receiver geometry); (2) noise-free, sparse data; (3) noisy data with a regular source/receiver geometry; and (4) noise-free data with dynamic source encoding.

Fig. 5a shows a slice of the 3D SEG/EAGE overthrust model. The model is composed of 187 grid points in depth and 801 grids points in the horizontal direction, with a grid size of 25 m in both directions. The initial model (Fig. 5b) is the smoothed version of the true model in Fig. 5a obtained using a strong Gaussian spatial filtering.

The original overthrust model is an acoustic model. For our elastic-waveform inversion, we build an S-wave velocity model using spatially varying V_p/V_s ratios as shown in Fig. 5b, resulting in an S-wave velocity model in Fig. 5c. Both the P- and S-wave velocity models contain sharp interfaces and smoothly varying regions.

We employ a total of 80 equally-spaced sources and 399 equally-spaced receivers at a depth of 50 m in the model. The source interval is 250 m and the receiver interval is 50 m. We use a Ricker wavelet with a center frequency of 8 Hz as the source wavelet. The source is vertical source force acted on the particle velocity wavefield. We employ the CG inversion framework for inversion. The initial P- and S-wave velocity models are shown in Figs. 6a and b, respectively. We also show the region of interest from the true velocity models in Figs. 7a and b for comparison of inversion results. We compare FWI inversion results obtained using the Tikhonov-FWI, TV-FWI

and TGPV-FWI.

In the first numerical test, we compare the results obtained using FWI with three different regularization schemes with all data of the 80 sources and the 399 receivers. The Tikhonov-FWI reconstructs smooth P- and S-wave velocity models as shown in Figs. 8a and b, respectively. The TV-FWI improves reconstruction of the interfaces and inversion resolution as depicted in Figs. 8c and d. By contrast, our TGPV-FWI produces best results among the three methods, as displayed in Figs. 8e and f. The method not only improves reconstruction of the interfaces, but also inversion accuracy. In addition, Figs. 8e and f contains fewer inversion artifacts than the other results in Fig. 8. Comparing between the inversion results obtained using the TV-FWI and our TGPV-FWI, we find that, the TV-FWI results contain staircase artifacts in regions between thin layers where seismic velocities vary smoothly in space. By contrast, our TGPV-FWI accurately reconstructs these smoothly varying velocities.

The comparison among the inversion results in Fig. 8 in the region of interest manifests the significant improvements of our TGPV-FWI compared with the other two FWI methods, as shown in Fig. 9.

In the second numerical test, we verify the efficacy of our TGPV-FWI for sparse seismic data acquired using inadequate numbers of sources and receivers. We use seismic data for one third of the sources (27 out of the 80 sources) and one third of the receivers (133 out of the 399 receivers) to conduct inversions. That is, we use only approximately 11 percent of the full dataset. The inversion results obtained using the three aforementioned inversion methods are shown in Fig. 10, and the zoom-in view of the inversion results in the region of interest are shown in Fig. 11. Both results of the Tikhonov-FWI and TV-FWI in Figs. 10a-d contain more inversion artifacts than those in Figs. 8a-d. By contrast, our TGPV-FWI results in Figs. 10e and f are almost identical to those in Figs. 8e and f. These inversion results demonstrate the capability of our TGPV-FWI to accurately reconstruct seismic velocities in complex models using sparse seismic data.

We conduct the third numerical test using noisy data. Fig. 12a shows the vertical component data of the 40th common-shot gather for the modified elastic SEG/EAGE overthrust model. Fig. 12b depicts the same vertical component data with random noise. The random noise obviously deteriorates the quality of the synthetic data, making many reflections indiscernible from the random noises. We also add the same level of random noise to the horizontal component.

We show the inversion results obtained using the Tikhonov-FWI, the TV-FWI and the TGPV-FWI in Fig. 13 and Fig. 14. In this case, the noises in the data leads to degraded inversion results compared with those in the previous two numerical tests. Nevertheless, our TGPV-FWI results shown in Figs. 14e and f are better than those produced with Tikhonov-FWI (Figs. 14a and b) and TV-FWI (Figs. 14c and d).

In the fourth numerical test, we adopt dynamic source encoding to verify the capability of our TGPV-FWI method. We form six encoded super gathers using the data for 80 sources, and dynamically encode the phase and amplitude of the super gathers with random time delays and random polarity reversal, respectively, over iterations. Fig. 15 and Fig. 16 show the inversion results for the aforementioned three FWI methods. The results show that our TGPV-FWI produces the most accurate inversion results among the three FWI methods.

Finally, we compare the convergences of the data and model misfits for the three FWI methods in Fig. 17. Fig. 17a shows the relative data misfits in the first numerical test using noise-free data with a regular source/receiver geometry. The data misfits of the Tikhonov-FWI and TV-FWI differ from each other insignificantly. By contrast, the data misfit for our TGPV-FWI decreases to a much smaller value than those of the other two methods. The corresponding data misfits in Fig. 17b for the noise-free, sparse data resemble the results in Fig. 17a.

Model misfit is another important indicator for FWI convergence. The model misfits in Fig. 17c and d for FWI with the Tikhonov, TV and TGPV regularizations and the sparse seismic data demonstrate again that our TGPV regularization is the most effective among the three regularization schemes. The P- and S-wave velocity model misfits for the source-encoding FWI test displayed in Fig. 17c and d, respectively, indicate that the model misfits for the source-encoding TGPV-FWI are always smaller than those for the other two inversion methods.

3.3 Field data example: Soda Lake geothermal field

We apply our TGPV-FWI method to surface seismic data acquired at the Soda Lake geothermal field in Nevada, USA, and compare the result with those obtained using the Tikhonov-FWI and TV-FWI.

Fig. 18a is a 2D P-wave velocity model for the Soda Lake geothermal field built using migration

velocity analysis. The high-velocity body at the center of the model is a basalt body. The near surface velocity is approximately 1455 m/s. The center frequency of the surface seismic data is approximately 35 Hz. There are a total of 62 shots along this 2D survey line. The source interval varies from approximately 30 m to 200 m. The receiver interval is approximately 66 m. Each common-shot gather contains 15 receivers to 46 receivers. Therefore, this dataset is considered to be very sparse in terms of data coverage.

Fig. 18b, c and d are the inverted velocity models produced using Tikhonov-FWI, TV-FWI, and TGPV-FWI. Comparing these three results, we find that Tikhonov-FWI produces only a low-resolution velocity model without many structural details, particularly in the region beneath the basalt body.

The TV-FWI result in Fig. 18b provides more details compared with that of Tikhonov-FWI in Fig. 18a. The TGPV-FWI result in Fig. 18c has the highest resolution among the three results.

The accuracy of FWI with field seismic data can be validated using the convergence curve of the data misfit. We plot the convergence curves of the data misfits for the Tikhonov-FWI, TV-FWI, and our TGPV-FWI of the field seismic data in Fig. 19, showing that our TGPV-FWI converges fastest and to the smallest value after 100 iterations among the three methods.

4 Conclusions

We have developed a novel full-waveform inversion method for acoustic and elastic waves using a total generalized p-variation regularization scheme. We decompose the regularized full-waveform inversion problem into two interlacing minimization problems. The first minimization problem is a conventional full-waveform inversion with a Tikhonov regularization term, and the second minimization problem is a denoising problem using the ℓ_p -norm total generalized variation. We have developed an efficient algorithm to solve the second minimization problem based on the split-Bregman iteration method. We have used two synthetic data examples and one field data example to verify the improved accuracy of our new method for both acoustic and elastic full-waveform inversion. Our numerical results demonstrate that our new acoustic and elastic full-waveform inversion with the total generalized p-variation regularization produces accurate inversion results that preserve both sharp interfaces and smooth background velocity variations in

the model. In addition, our new inversion method produces reliable inversion results when using sparse seismic data, noisy data, and dynamic source encoding. Our results of synthetic and field seismic data demonstrate that our new inversion method can be used as a robust and accurate tool for subsurface velocity model building, subsurface reservoir characterization, and large-scale tomographic reconstruction using Earthquake data.

5 Acknowledgments

This work was supported by U.S. Department of Energy through contract DE-AC52-06NA25396 to Los Alamos National Laboratory (LANL). The computation was performed using the supercomputers of LANL's Institutional Computing Program. We thank Benxin Chi of LANL and Rick Chartrand of Descartes Labs for helpful discussions. Surface seismic data from the Soda Lake geothermal field was provided by Magma Energy (U.S.) Corp.

References

- Anagaw, A., 2011, Full waveform inversion with total variation regularization: Proceedings of the 2011 CSPG CSEG CWLS Joint Annual Convention, 1–4.
- Asnaashari, A., R. Brossier, S. Garambois, F. Audebert, P. Thore, and J. Virieux, 2013, Regularized seismic full waveform inversion with prior model information: *Geophysics*, **78**, R25–R36.
- Bozdağ, E., J. Trampert, and J. Tromp, 2011, Misfit functions for full waveform inversion based on instantaneous phase and envelope measurements: *Geophysical Journal International*, **185**, 845–870.
- Bredies, K., K. Kunisch, and T. Pock, 2010, Total generalized variation: *SIAM Journal of Imaging Science*, **3**, 492–526.
- Candes, E. J., J. Romberg, and T. Tao, 2006, Robust uncertainty principles: exact signal reconstruction from highly incomplete frequency information: *IEEE Transactions on Information Theory*, **52**, 489–509.
- Candes, E. J., and M. B. Wakin, 2008, An introduction to compressive sampling: *IEEE Signal Processing Magazine*, **25**, 21–30.

- Chartrand, R., 2009, Fast algorithms for nonconvex compressive sensing: MRI reconstruction from very few data: 2009 IEEE International Symposium on Biomedical Imaging: From Nano to Macro, 262–265.
- Chartrand, R., E. Y. Sidky, and X. Pan, 2013, Nonconvex compressive sensing for X-ray CT: An algorithm comparison: 2013 Asilomar Conference on Signals, Systems and Computers, 665–669.
- Chi, B., L. Dong, and Y. Liu, 2014, Full waveform inversion method using envelope objective function without low frequency data: *Journal of Applied Geophysics*, **109**, 36 – 46.
- , 2015, Correlation-based reflection full-waveform inversion: *Geophysics*, **80**, R189–R202.
- Choi, Y., and T. Alkhalifah, 2016, An optimized correlation-based full waveform inversion: EAGE Technical Programme Extended Abstracts 2016, 1–5.
- Donoho, D. L., 2006, Compressed sensing: *IEEE Transactions on Information Theory*, **52**, 1289–1306.
- Epanomeritakis, I., V. Akelik, O. Ghattas, and J. Bielak, 2008, A Newton-CG method for large-scale three-dimensional elastic full-waveform seismic inversion: *Inverse Problems*, **24**, 034015.
- Esser, E., L. Guasch, F. J. Herrmann, and M. Warner, 2016, Constrained waveform inversion for automatic salt flooding: *The Leading Edge*, **35**, 235–239.
- Fichtner, A., and J. Trampert, 2011, Hessian kernels of seismic data functionals based upon adjoint techniques: *Geophysical Journal International*, **185**, 775–798.
- Goldstein, T., and S. Osher, 2009, The split Bregman method for L1-regularized problems: *SIAM Journal on Imaging Sciences*, **2**, 323–343.
- Guitton, A., 2012, Blocky regularization schemes for Full-Waveform Inversion: *Geophysical Prospecting*, **60**, 870–884.
- Guitton, A., G. Ayeni, and E. Díaz, 2012, Constrained full-waveform inversion by model reparameterization: *Geophysics*, **77**, R117–R127.
- Guitton, A., and W. W. Symes, 2003, Robust inversion of seismic data using the huber norm: *Geophysics*, **68**, 1310–1319.
- Ha, T., W. Chung, and C. Shin, 2009, Waveform inversion using a back-propagation algorithm and a huber function norm: *Geophysics*, **74**, R15–R24.
- Hale, D., 2007, Local dip filtering with directional laplacians: Center for Wave Phenomena reports.

- Jiao, K., D. Sun, X. Cheng, and D. Vigh, 2015, Adjustive full waveform inversion: SEG Technical Program Expanded Abstracts 2015, 1091–1095.
- Knoll, F., K. Bredies, T. Pock, and R. Stollberger, 2011, Second order total generalized variation (TGV) for MRI: *Magnetic Resonance in Medicine*, **65**, 480–491.
- Lewis, W., D. Amazonas, D. Vigh, and R. Coates, 2014, Geologically constrained full-waveform inversion using an anisotropic diffusion based regularization scheme: Application to a 3D off-shore Brazil dataset: SEG Technical Program Expanded Abstracts 2014, 1083–1088.
- Lin, Y., and L. Huang, 2014, Acoustic- and elastic-waveform inversion using a modified total-variation regularization scheme: *Geophysical Journal International*, **200**, 489–502.
- Luo, S., and P. Sava, 2011, A deconvolution-based objective function for wave-equation inversion: SEG Technical Program Expanded Abstracts 2011, 2788–2792.
- Luo, Y., Y. Ma, Y. Wu, H. Liu, and L. Cao, 2016, Full-traveltime inversion: *Geophysics*, **81**, R261–R274.
- Luo, Y., and G. T. Schuster, 1991, Wave-equation traveltime inversion: *Geophysics*, **56**, 645–653.
- Ma, Y., and D. Hale, 2013, Wave-equation reflection traveltime inversion with dynamic warping and full-waveform inversion: *Geophysics*, **78**, R223–R233.
- Métivier, L., R. Brossier, Q. Mérigot, E. Oudet, and J. Virieux, 2016a, Measuring the misfit between seismograms using an optimal transport distance: application to full waveform inversion: *Geophysical Journal International*, **205**, 345–377.
- , 2016b, An optimal transport approach for seismic tomography: application to 3d full waveform inversion: *Inverse Problems*, **32**, 115008.
- Métivier, L., R. Brossier, S. Operto, and J. Virieux, 2017, Full waveform inversion and the truncated newton method: *SIAM Review*, **59**, 153–195.
- Métivier, L., R. Brossier, J. Virieux, and S. Operto, 2013, Full waveform inversion and the truncated newton method: *SIAM Journal on Scientific Computing*, **35**, B401–B437.
- Mora, P., 1987, Nonlinear two-dimensional elastic inversion of multioffset seismic data: *Geophysics*, **52**, 1211–1228.
- , 1988, Elastic wave-field inversion of reflection and transmission data: *Geophysics*, **53**, 750–759.
- Nocedal, J., and S. J. Wright, 2006, *Numerical Optimization*, 2 ed.: Springer, New York.

- Pan, W., K. A. Innanen, G. F. Margrave, and D. Cao, 2015, Efficient pseudo-Gauss-Newton full-waveform inversion in the $\tau - p$ domain: *Geophysics*, **80**, R225–R14.
- Pan, W., K. A. Innanen, G. F. Margrave, M. C. Fehler, X. Fang, and J. Li, 2016, Estimation of elastic constants for HTI media using Gauss-Newton and full-Newton multiparameter full-waveform inversion: *Geophysics*, **81**, R275–R291.
- Pratt, G., C. Shin, and Hicks, 1998, Gauss-newton and full newton methods in frequency-space seismic waveform inversion: *Geophysical Journal International*, **133**, 341–362.
- Rudin, L. I., S. Osher, and E. Fatemi, 1992, Nonlinear total variation based noise removal algorithms: *Physica D: Nonlinear Phenomena*, **60**, 259 – 268.
- Tang, Y., and S. Lee, 2010, Preconditioning full waveform inversion with phaseencoded hessian: SEG Technical Program Expanded Abstracts 2010, 1034–1038.
- Tarantola, A., 1984, Inversion of seismic reflection data in the acoustic approximation: *Geophysics*, **49**, 1259–1266.
- , 1986, A strategy for nonlinear elastic inversion of seismic reflection data: *Geophysics*, **51**, 1893–1903.
- Tikhonov, A., A. Goncharsky, V. Stepanov, and A. Yagola, 1995, Numerical methods for the solution of ill-posed problems: Springer.
- Van Leeuwen, T., and W. A. Mulder, 2010, A correlation-based misfit criterion for wave-equation travelttime tomography: *Geophysical Journal International*, **182**, 1383–1394.
- Virieux, J., and S. Operto, 2009, An overview of full-waveform inversion in exploration geophysics: *Geophysics*, **74**, WCC1–WCC26.
- Warner, M., and L. Guasch, 2016, Adaptive waveform inversion: Theory: *Geophysics*, **81**, R429–R445.
- Wu, R.-S., J. Luo, and B. Wu, 2014, Seismic envelope inversion and modulation signal model: *Geophysics*, **79**, WA13–WA24.
- Xue, Z., H. Zhu, and S. Fomel, 2017, Full-waveform inversion using seislet regularization: *Geophysics*, **82**, A43–A49.
- Yang, Y., B. Engquist, J. Sun, and B. D. Froese, 2017, Application of optimal transport and the quadratic wasserstein metric to full-waveform inversion: *Geophysics*, **0**, 1–103.
- Yang, Y., B. Engquist, J. Sun, and B. F. Hamfeldt, 2018, Application of optimal transport and the

- quadratic Wasserstein metric to full-waveform inversion: *Geophysics*, **83**, R43–R62.
- Zhang, H., L. Wang, B. Yan, L. Li, A. Cai, and G. Hu, 2016, Constrained total generalized p-variation minimization for few-view X-Ray computed tomography image reconstruction: *PLOS ONE*, **11**, e0149899+.
- Zhang, Z., L. Huang, and Y. Lin, 2012, A wave-energy-based precondition approach to full-waveform inversion in the time domain: *SEG Technical Program Expanded Abstracts*, **485**, 1–5.
- Zhdanov, M., 2002, *Geophysical inverse theory and regularization problems*, 1 ed.: Elsevier Science.

Appendix A: Solution to the second minimization problem in the 2D case

Eq. (7b) is equivalent to the following problem:

$$\{\mathbf{u}^*, \mathbf{w}^*, \mathbf{h}^*, \mathbf{s}^*\} = \arg \min_{\mathbf{u}, \mathbf{w}, \mathbf{h}, \mathbf{s}} \left\{ \frac{\mu}{2} \|\mathbf{m}^{(l+1)} - \mathbf{u}\|_2^2 + \alpha_0 \|\mathbf{h}\|_p^p + \alpha_1 \|\mathbf{s}\|_p^p \right\}, \quad (\text{A-9})$$

$$\text{s.t. } \mathbf{h} = \begin{bmatrix} \mathbf{h}_x \\ \mathbf{h}_y \end{bmatrix} = \nabla \mathbf{u} - \mathbf{w}, \quad (\text{A-10})$$

$$\mathbf{s} = \begin{bmatrix} \mathbf{s}_{xx} & \mathbf{s}_{xy} \\ \mathbf{s}_{xy} & \mathbf{s}_{yy} \end{bmatrix} = \boldsymbol{\varepsilon}(\mathbf{w}), \quad (\text{A-11})$$

where \mathbf{h} and \mathbf{s} are dual variables, $\mu = 1/\lambda_2$ is a parameter chosen for convenience, and $\mathbf{w} = [\mathbf{w}_x, \mathbf{w}_y]^T$.

Using the split-Bregman iteration technique (Goldstein and Osher, 2009; Chartrand, 2009), we reformulate the constrained minimization problem as the following optimization system:

$$\begin{aligned} \left\{ \mathbf{u}^{(k+1)}, \mathbf{w}^{(k+1)}, \mathbf{h}^{(k+1)}, \mathbf{s}^{(k+1)} \right\} = \arg \min_{\mathbf{u}, \mathbf{w}, \mathbf{h}, \mathbf{s}} \left\{ \alpha_0 \|\mathbf{h}\|_p + \frac{\eta_0}{2} \|\mathbf{h} - \tilde{\mathbf{h}}^{(k)} - (\nabla \mathbf{u} - \mathbf{w})\|_2^2 \right. \\ \left. + \alpha_1 \|\mathbf{s}\|_p^p + \frac{\eta_1}{2} \|\mathbf{s} - \tilde{\mathbf{s}}^{(k)} - \boldsymbol{\varepsilon}(\mathbf{w})\|_2^2 + \frac{\mu}{2} \|\mathbf{u} - \mathbf{m}^{(l+1)}\|_2^2 \right\}, \end{aligned} \quad (\text{A-12})$$

$$\tilde{\mathbf{h}}^{(k+1)} = \tilde{\mathbf{h}}^{(k)} + \left[(\nabla \mathbf{u}^{(k+1)} - \mathbf{w}^{(k+1)}) - \mathbf{h}^{(k+1)} \right], \quad (\text{A-13})$$

$$\tilde{\mathbf{s}}^{(k+1)} = \tilde{\mathbf{s}}^{(k)} + \left[\boldsymbol{\varepsilon}(\mathbf{w}^{(k+1)}) - \mathbf{s}^{(k+1)} \right], \quad (\text{A-14})$$

where $\tilde{\mathbf{h}}$ and $\tilde{\mathbf{s}}$ are auxiliary split-Bregman variables. Note that in the above formulation, l is the index of FWI inversion iteration, while k is the index of the split-Bregman iteration in the second minimization problem. In addition, η_0 and η_1 are two regularization parameters for the constrained minimization problem in eq. (A-12).

We formulate the following four subproblems associated with the variables \mathbf{h} , \mathbf{s} , \mathbf{u} and \mathbf{w} from eq. (A-12).

The first subproblem is the minimization of \mathbf{u} :

$$\arg \min_{\mathbf{u}} \left\{ \frac{\mu}{2} \|\mathbf{u} - \mathbf{m}^{(l+1)}\|_2^2 + \frac{\eta_0}{2} \|\mathbf{h} - \tilde{\mathbf{h}} - (\nabla \mathbf{u} - \mathbf{w})\|_2^2 \right\}. \quad (\text{A-15})$$

The first-order optimality condition of eq. (A-15) is

$$(\mu \mathbf{I} - \eta_0 \nabla^T \nabla) \mathbf{u}^{(k+1)} = \mu \mathbf{m}^{(l+1)} + \eta_0 \nabla_x^T (\mathbf{h}_x + \mathbf{w}_x - \tilde{\mathbf{h}}_x) + \eta_0 \nabla_y^T (\mathbf{h}_y + \mathbf{w}_y - \tilde{\mathbf{h}}_y). \quad (\text{A-16})$$

Because the linear system in eq. (A-16) is strictly diagonally dominant, it can be efficiently solved with the Gauss-Seidel iteration:

$$\begin{aligned} \mathbf{u}_{i,j}^{(k+1)} &= \frac{\eta_0}{\mu + 4\eta_0} \left[\mathbf{u}_{i+1,j}^{(k)} + \mathbf{u}_{i-1,j}^{(k)} + \mathbf{u}_{i,j+1}^{(k)} + \mathbf{u}_{i,j-1}^{(k)} \right] \\ &+ \frac{\eta_0}{\mu + 4\eta_0} \left[\mathbf{h}_{x|i-1,j}^{(k)} - \mathbf{h}_{x|i,j}^{(k)} + \mathbf{w}_{x|i-1,j}^{(k)} - \mathbf{w}_{x|i,j}^{(k)} - \left(\tilde{\mathbf{h}}_{x|i-1,j}^{(k)} - \tilde{\mathbf{h}}_{x|i,j}^{(k)} \right) \right] \\ &+ \frac{\eta_0}{\mu + 4\eta_0} \left[\mathbf{h}_{y|i,j-1}^{(k)} - \mathbf{h}_{y|i,j}^{(k)} + \mathbf{w}_{y|i,j-1}^{(k)} - \mathbf{w}_{y|i,j}^{(k)} - \left(\tilde{\mathbf{h}}_{y|i,j-1}^{(k)} - \tilde{\mathbf{h}}_{y|i,j}^{(k)} \right) \right] \\ &+ \frac{\mu}{\mu + 4\eta_0} \mathbf{m}_{i,j}^{(l+1)} \end{aligned} \quad (\text{A-17})$$

Goldstein and Osher (2009) developed a similar solution for the total-variation image denoising problem.

The second subproblem is the minimization of \mathbf{w} :

$$\arg \min_{\mathbf{w}} \left\{ \frac{\eta_0}{2} \|\mathbf{h} - \tilde{\mathbf{h}} - (\nabla \mathbf{u} - \mathbf{w})\|_2^2 + \frac{\eta_1}{2} \|\mathbf{s} - \tilde{\mathbf{s}} - \varepsilon(\mathbf{w})\|_2^2 \right\}. \quad (\text{A-18})$$

The first-order optimality condition of eq. (A-18) leads to two linear systems:

$$\begin{aligned} (\eta_0 \mathbf{I} - \eta_1 \nabla_x^T \nabla_x - \frac{1}{2} \eta_1 \nabla_y^T \nabla_y) \mathbf{w}_x &= -\eta_0 (\mathbf{h}_x - \tilde{\mathbf{h}}_x - \nabla_x \mathbf{u}) + \eta_1 \nabla_x^T (\mathbf{s}_{xx} - \tilde{\mathbf{s}}_{xx}) \\ &+ \eta_1 \nabla_y^T (\mathbf{s}_{xy} - \tilde{\mathbf{s}}_{xy} - \frac{1}{2} \nabla_x \mathbf{w}_y), \end{aligned} \quad (\text{A-19})$$

$$\begin{aligned} (\eta_0 \mathbf{I} - \frac{1}{2} \eta_1 \nabla_x^T \nabla_x - \eta_1 \nabla_y^T \nabla_y) \mathbf{w}_y &= -\eta_0 (\mathbf{h}_y - \tilde{\mathbf{h}}_y - \nabla_y \mathbf{u}) + \eta_1 \nabla_y^T (\mathbf{s}_{yy} - \tilde{\mathbf{s}}_{yy}) \\ &+ \eta_1 \nabla_x^T (\mathbf{s}_{xy} - \tilde{\mathbf{s}}_{xy} - \frac{1}{2} \nabla_y \mathbf{w}_x), \end{aligned} \quad (\text{A-20})$$

which can also be solved via the Gauss-Seidel iteration because of their strict diagonal dominance. We use eq. (A-19) to explain the procedure, and the solution to eq. (A-20) can be obtained analogously.

For convenience, we first define and compute an intermediate variable $\mathbf{v}_{y,x}$ for $\nabla_x \mathbf{w}_y$ as

$$\mathbf{v}_{y,x|i,j}^{(k)} = \mathbf{w}_{y|i+1,j}^{(k)} - \mathbf{w}_{y|i,j}^{(k)}. \quad (\text{A-21})$$

We then obtain

$$\mathbf{w}_{x|i,j}^{(k+1)} = \frac{\eta_1}{\eta_0 + 3\eta_1} \left[\mathbf{w}_{x|i+1,j}^{(k)} + \mathbf{w}_{x|i-1,j}^{(k)} + \frac{1}{2} \left(\mathbf{w}_{x|i,j+1}^{(k)} + \mathbf{w}_{x|i,j-1}^{(k)} \right) \right]$$

$$\begin{aligned}
& - \frac{\eta_0}{\eta_0 + 3\eta_1} \left[\mathbf{h}_{x|i,j}^{(k)} - \tilde{\mathbf{h}}_{x|i,j}^{(k)} - \left(\mathbf{u}_{i+1,j}^{(k+1)} - \mathbf{u}_{i,j}^{(k+1)} \right) \right] \\
& + \frac{\eta_1}{\eta_0 + 3\eta_1} \left[\mathbf{s}_{xx|i-1,j}^{(k)} - \mathbf{s}_{xx|i,j}^{(k)} - \left(\tilde{\mathbf{s}}_{xx|i-1,j}^{(k)} - \tilde{\mathbf{s}}_{xx|i,j}^{(k)} \right) \right] \\
& + \frac{\eta_1}{\eta_0 + 3\eta_1} \left[\mathbf{s}_{xy|i,j-1}^{(k)} - \mathbf{s}_{xy|i,j}^{(k)} - \left(\tilde{\mathbf{s}}_{xy|i,j-1}^{(k)} - \tilde{\mathbf{s}}_{xy|i,j}^{(k)} \right) - \frac{1}{2} \left(\mathbf{v}_{y,x|i,j-1}^{(k)} - \mathbf{v}_{y,x|i,j}^{(k)} \right) \right]. \tag{A-22}
\end{aligned}$$

The third subproblem is the minimization of \mathbf{h} :

$$\arg \min_{\mathbf{h}} \left\{ \alpha_0 \|\mathbf{h}\|_p^p + \frac{\eta_0}{2} \|\mathbf{h} - \tilde{\mathbf{h}} - (\nabla \mathbf{u} - \mathbf{w})\|_2^2 \right\}. \tag{A-23}$$

This problem can be efficiently solved with

$$\mathbf{h}^{(k+1)} = \mathcal{S}_p \left((\nabla \mathbf{u}^{(k+1)} - \mathbf{w}^{(k+1)}) + \tilde{\mathbf{h}}^{(k)}, \frac{\alpha_0}{\eta_0} \right), \tag{A-24}$$

where the generalized p -shrinkage \mathcal{S}_p reads (Chartrand et al., 2013)

$$\mathcal{S}_p \left(\xi, \frac{1}{\beta} \right) = \max(|\xi| - \beta^{p-2} |\xi|^{p-1}, 0) \frac{\xi}{|\xi|}. \tag{A-25}$$

The shrinkage operation is an element-wise operation and therefore can be solved with fairly small computational cost.

The fourth subproblem is the minimization of \mathbf{s} :

$$\arg \min_{\mathbf{s}} \left\{ \alpha_1 \|\mathbf{s}\|_p^p + \frac{\eta_1}{2} \|\mathbf{s} - \tilde{\mathbf{s}} - \varepsilon(\mathbf{w})\|_2^2 \right\}. \tag{A-26}$$

which can also be solved with the generalized p -shrinkage:

$$\mathbf{s}^{(k+1)} = \mathcal{S}_p \left(\varepsilon(\mathbf{w}^{(k+1)}) + \tilde{\mathbf{s}}^{(k)}, \frac{\alpha_1}{\eta_1} \right) \tag{A-27}$$

Lastly, the update of the auxiliary split-Bregman variables is trivial. For example, for $\tilde{\mathbf{h}}$, we have

$$\tilde{\mathbf{h}}_{x|i,j}^{(k+1)} = \tilde{\mathbf{h}}_{x|i,j}^{(k)} + \left(\mathbf{u}_{i+1,j}^{(k+1)} - \mathbf{u}_{i,j}^{(k+1)} - \mathbf{w}_{x|i,j}^{(k+1)} - \mathbf{h}_{x|i,j}^{(k+1)} \right), \tag{A-28}$$

$$\tilde{\mathbf{h}}_{y|i,j}^{(k+1)} = \tilde{\mathbf{h}}_{y|i,j}^{(k)} + \left(\mathbf{u}_{i,j+1}^{(k+1)} - \mathbf{u}_{i,j}^{(k+1)} - \mathbf{w}_{y|i,j}^{(k+1)} - \mathbf{h}_{y|i,j}^{(k+1)} \right). \tag{A-29}$$

And the update of the auxiliary $\tilde{\mathbf{s}}$ is similar.

Appendix B: Solution to the second minimization problem in the 3D case

In the 3D case, the TGPV regularization term in eq. (1) reads:

$$\mathcal{T}_p(\mathbf{m}) = \arg \min_{\mathbf{w}} \alpha_0 \|\nabla \mathbf{m} - \mathbf{w}\|_p^p + \alpha_1 \|\varepsilon(\mathbf{w})\|_p^p, \quad (0 < p < 1) \quad (\text{B-1})$$

where the gradient is

$$\nabla \mathbf{m} = \begin{bmatrix} \nabla_x \mathbf{m} \\ \nabla_y \mathbf{m} \\ \nabla_z \mathbf{m} \end{bmatrix}, \quad (\text{B-2})$$

and the symmetric gradient $\varepsilon(\cdot)$ is

$$\varepsilon(\mathbf{w}) = \begin{bmatrix} \nabla_x \mathbf{w}_x & \frac{1}{2}(\nabla_x \mathbf{w}_y + \nabla_y \mathbf{w}_x) & \frac{1}{2}(\nabla_x \mathbf{w}_z + \nabla_z \mathbf{w}_x) \\ \frac{1}{2}(\nabla_x \mathbf{w}_y + \nabla_y \mathbf{w}_x) & \nabla_y \mathbf{w}_y & \frac{1}{2}(\nabla_y \mathbf{w}_z + \nabla_z \mathbf{w}_y) \\ \frac{1}{2}(\nabla_x \mathbf{w}_z + \nabla_z \mathbf{w}_x) & \frac{1}{2}(\nabla_y \mathbf{w}_z + \nabla_z \mathbf{w}_y) & \nabla_z \mathbf{w}_z \end{bmatrix}. \quad (\text{B-3})$$

We still use a dual-variable alternating-direction minimization strategy to solve the regularized FWI. We transform the second minimization problem to

$$\arg \min_{\mathbf{u}, \mathbf{w}, \mathbf{h}, \mathbf{s}} \frac{\mu}{2} \|\mathbf{u} - \mathbf{m}^{(k+1)}\|_2^2 + \alpha_0 \|\mathbf{h}\|_p^p + \alpha_1 \|\mathbf{s}\|_p^p, \quad (\text{B-4})$$

$$\text{s.t. } \mathbf{h} = \begin{bmatrix} \mathbf{h}_x \\ \mathbf{h}_y \\ \mathbf{h}_z \end{bmatrix} = \nabla \mathbf{u} - \mathbf{w}, \quad (\text{B-5})$$

$$\mathbf{s} = \begin{bmatrix} \mathbf{s}_{xx} & \mathbf{s}_{xy} & \mathbf{s}_{xz} \\ \mathbf{s}_{xy} & \mathbf{s}_{yy} & \mathbf{s}_{yz} \\ \mathbf{s}_{xz} & \mathbf{s}_{yz} & \mathbf{s}_{zz} \end{bmatrix} = \varepsilon(\mathbf{w}), \quad (\text{B-6})$$

which also contains four subproblems as is in the 2D case.

The first-order optimality condition for the minimization of variable \mathbf{u} is

$$(\mu \mathbf{I} - \eta_0 \nabla^T \nabla) \mathbf{u}^{(k+1)} = \mu \mathbf{m}^{(k+1)} + \eta_0 \nabla_x^T (\mathbf{h}_x + \mathbf{w}_x - \tilde{\mathbf{h}}_x) + \eta_0 \nabla_y^T (\mathbf{h}_y + \mathbf{w}_y - \tilde{\mathbf{h}}_y) + \eta_0 \nabla_z^T (\mathbf{h}_z + \mathbf{w}_z - \tilde{\mathbf{h}}_z). \quad (\text{B-7})$$

The Gauss-Seidel solution to this linear system is

$$\begin{aligned}
\mathbf{u}_{i,j,k}^{(k+1)} &= \frac{\eta_0}{\mu + 6\eta_0} \left[\mathbf{u}_{i+1,j,k}^{(k)} + \mathbf{u}_{i-1,j,k}^{(k)} + \mathbf{u}_{i,j+1,k}^{(k)} + \mathbf{u}_{i,j-1,k}^{(k)} + \mathbf{u}_{i,j,k+1}^{(k)} + \mathbf{u}_{i,j,k-1}^{(k)} \right] \\
&+ \frac{\eta_0}{\mu + 6\eta_0} \left[\mathbf{h}_{x|i-1,j,k}^{(k)} - \mathbf{h}_{x|i,j,k}^{(k)} + \mathbf{w}_{x|i-1,j,k}^{(k)} - \mathbf{w}_{x|i,j,k}^{(k)} - (\tilde{\mathbf{h}}_{x|i-1,j,k}^{(k)} - \tilde{\mathbf{h}}_{x|i,j,k}^{(k)}) \right] \\
&+ \frac{\eta_0}{\mu + 6\eta_0} \left[\mathbf{h}_{y|i,j-1,k}^{(k)} - \mathbf{h}_{y|i,j,k}^{(k)} + \mathbf{w}_{y|i,j-1,k}^{(k)} - \mathbf{w}_{y|i,j,k}^{(k)} - (\tilde{\mathbf{h}}_{y|i,j-1,k}^{(k)} - \tilde{\mathbf{h}}_{y|i,j,k}^{(k)}) \right] \\
&+ \frac{\eta_0}{\mu + 6\eta_0} \left[\mathbf{h}_{z|i,j,k-1}^{(k)} - \mathbf{h}_{z|i,j,k}^{(k)} + \mathbf{w}_{z|i,j,k-1}^{(k)} - \mathbf{w}_{z|i,j,k}^{(k)} - (\tilde{\mathbf{h}}_{z|i,j,k-1}^{(k)} - \tilde{\mathbf{h}}_{z|i,j,k}^{(k)}) \right] \\
&+ \frac{\mu}{\mu + 6\eta_0} \mathbf{m}_{i,j,k}^{(k+1)}. \tag{B-8}
\end{aligned}$$

The first-order optimality condition for the minimization of variable \mathbf{w} is a system composed of three equations:

$$\begin{aligned}
(\eta_0 \mathbf{I} - \eta_1 \nabla_x^T \nabla_x - \frac{1}{2} \eta_1 \nabla_y^T \nabla_y - \frac{1}{2} \eta_1 \nabla_z^T \nabla_z) \mathbf{w}_x &= -\eta_0 (\mathbf{h}_x - \tilde{\mathbf{h}}_x - \nabla_x \mathbf{u}) \\
&+ \eta_1 \nabla_x^T (\mathbf{s}_{xx} - \tilde{\mathbf{s}}_{xx}) \\
&+ \eta_1 \nabla_y^T (\mathbf{s}_{xy} - \tilde{\mathbf{s}}_{xy} - \frac{1}{2} \nabla_x \mathbf{w}_y) \\
&+ \eta_1 \nabla_z^T (\mathbf{s}_{xz} - \tilde{\mathbf{s}}_{xz} - \frac{1}{2} \nabla_x \mathbf{w}_z), \tag{B-9}
\end{aligned}$$

$$\begin{aligned}
(\eta_0 \mathbf{I} - \frac{1}{2} \eta_1 \nabla_x^T \nabla_x - \eta_1 \nabla_y^T \nabla_y - \frac{1}{2} \eta_1 \nabla_z^T \nabla_z) \mathbf{w}_y &= -\eta_0 (\mathbf{h}_y - \tilde{\mathbf{h}}_y - \nabla_y \mathbf{u}) \\
&+ \eta_1 \nabla_x^T (\mathbf{s}_{xy} - \tilde{\mathbf{s}}_{xy} - \frac{1}{2} \nabla_y \mathbf{w}_x) \\
&+ \eta_1 \nabla_y^T (\mathbf{s}_{yy} - \tilde{\mathbf{s}}_{yy}) \\
&+ \eta_1 \nabla_z^T (\mathbf{s}_{yz} - \tilde{\mathbf{s}}_{yz} - \frac{1}{2} \nabla_y \mathbf{w}_z), \tag{B-10}
\end{aligned}$$

$$\begin{aligned}
(\eta_0 \mathbf{I} - \frac{1}{2} \eta_1 \nabla_x^T \nabla_x - \frac{1}{2} \eta_1 \nabla_y^T \nabla_y - \eta_1 \nabla_z^T \nabla_z) \mathbf{w}_z &= -\eta_0 (\mathbf{h}_z - \tilde{\mathbf{h}}_z - \nabla_z \mathbf{u}) \\
&+ \eta_1 \nabla_x^T (\mathbf{s}_{xz} - \tilde{\mathbf{s}}_{xz} - \frac{1}{2} \nabla_z \mathbf{w}_x) \\
&+ \eta_1 \nabla_y^T (\mathbf{s}_{yz} - \tilde{\mathbf{s}}_{yz} - \frac{1}{2} \nabla_z \mathbf{w}_y) \\
&+ \eta_1 \nabla_z^T (\mathbf{s}_{zz} - \tilde{\mathbf{s}}_{zz}). \tag{B-11}
\end{aligned}$$

Solutions to the above three minimization equations can be obtained with the Gauss-Seidel iteration analogously to those for the 2D case. For instance, for the first equation (B-9), we first define and compute two intermediate variables $\mathbf{v}_{y,x}$ for $\nabla_x \mathbf{w}_y$ and $\mathbf{v}_{z,x}$ for $\nabla_x \mathbf{w}_z$ as

$$\mathbf{v}_{y,x|i,j,k}^{(k)} = \mathbf{w}_{y|i+1,j,k}^{(k)} - \mathbf{w}_{y|i,j,k}^{(k)}, \tag{B-12}$$

$$\mathbf{v}_{z,x|i,j,k}^{(k)} = \mathbf{w}_{z|i+1,j,k}^{(k)} - \mathbf{w}_{z|i,j,k}^{(k)}. \quad (\text{B-13})$$

We then obtain

$$\begin{aligned} \mathbf{w}_{x|i,j,k}^{(k+1)} = & \frac{\eta_1}{\eta_0 + 4\eta_1} \left[\mathbf{w}_{x|i+1,j,k}^{(k)} + \mathbf{w}_{x|i-1,j,k}^{(k)} + \frac{1}{2} \left(\mathbf{w}_{x|i,j+1,k}^{(k)} + \mathbf{w}_{x|i,j-1,k}^{(k)} \right) + \frac{1}{2} \left(\mathbf{w}_{x|i,j,k+1}^{(k)} + \mathbf{w}_{x|i,j,k-1}^{(k)} \right) \right] \\ & - \frac{\eta_0}{\eta_0 + 4\eta_1} \left[\mathbf{h}_{x|i,j,k}^{(k)} - \tilde{\mathbf{h}}_{x|i,j,k}^{(k)} - \left(\mathbf{u}_{i+1,j,k}^{(k+1)} - \mathbf{u}_{i,j,k}^{(k+1)} \right) \right] \\ & + \frac{\eta_1}{\eta_0 + 4\eta_1} \left[\mathbf{s}_{xx|i-1,j,k}^{(k)} - \mathbf{s}_{xx|i,j,k}^{(k)} - \left(\tilde{\mathbf{s}}_{xx|i-1,j,k}^{(k)} - \tilde{\mathbf{s}}_{xx|i,j,k}^{(k)} \right) \right] \\ & + \frac{\eta_1}{\eta_0 + 4\eta_1} \left[\mathbf{s}_{xy|i,j-1,k}^{(k)} - \mathbf{s}_{xy|i,j,k}^{(k)} - \left(\tilde{\mathbf{s}}_{xy|i,j-1,k}^{(k)} - \tilde{\mathbf{s}}_{xy|i,j,k}^{(k)} \right) - \frac{1}{2} \left(\mathbf{v}_{y,x|i,j-1,k}^{(k)} - \mathbf{v}_{y,x|i,j,k}^{(k)} \right) \right] \\ & + \frac{\eta_1}{\eta_0 + 4\eta_1} \left[\mathbf{s}_{xz|i,j,k-1}^{(k)} - \mathbf{s}_{xz|i,j,k}^{(k)} - \left(\tilde{\mathbf{s}}_{xz|i,j,k-1}^{(k)} - \tilde{\mathbf{s}}_{xz|i,j,k}^{(k)} \right) - \frac{1}{2} \left(\mathbf{v}_{z,x|i,j,k-1}^{(k)} - \mathbf{v}_{z,x|i,j,k}^{(k)} \right) \right]. \end{aligned} \quad (\text{B-14})$$

Solutions to the other two equations can be obtained similarly.

The minimization problems for the other variables, including the split-Bregman variables, are trivial to solve.

Appendix C: Algorithm implementation of the TGPV-FWI

We summarize the algorithm of our TGPV-FWI in the following Algorithm 1.

Algorithm 1: TGPV-FWI.

input : Observed data \mathbf{d} , initial model $\mathbf{m}^{(0)}$, initial misfit $\varepsilon_0 = \text{HUGE_VALUE}$

while $\varepsilon > \varepsilon_{\min}$ **do**

- 1) Compute the adjoint source based on certain type of misfit function
- 2) Compute the gradient \mathbf{g}_k using the adjoint-state method
- 3) Solve the second subproblem for model $\mathbf{m}^{(k)}$:

input : $\mathbf{m}^{(k)}$, maximum number of split-Bregman iteration n_{\max} and m_{\max} , norm p , regularization parameter λ_2 (or equivalently $1/\mu$)

while $n < n_{\max}$ **do**

while $m < m_{\max}$ **do**

- 3.1.1) Minimization of \mathbf{u} using eq. (A-15)
- 3.1.2) Minimization of \mathbf{w} using eq. (A-18)
- 3.1.3) Minimization of \mathbf{h} using eq. (A-23)
- 3.1.4) Minimization of \mathbf{s} using eq. (A-26)

end

3.2.1) Update of the split-Bregman variable $\tilde{\mathbf{h}}$

3.2.2) Update of the split-Bregman variable $\tilde{\mathbf{s}}$

end

output: u

- 4) The Tikhonov regularization using

$$\mathbf{g}^{(k+1)} \leftarrow \mathbf{g}^{(k+1)} + \lambda_1 (\mathbf{m}^{(k+1)} - \mathbf{u}^{(k)})$$

- 5) Compute the search direction, say $\phi^{(k+1)}$, based on CG or L-BFGS framework
- 6) Compute the optimal step length β using the perturbation method or the line search method
- 7) Update the model using the computed search direction $\phi^{(k+1)}$ and the optimal step length β

end

output: The updated model \mathbf{m}_N (or equivalently \mathbf{u}_N)

In Step (3) of this algorithm, n_{\max} is the maximum number of the outer split-Bregman iterations, which can also be replaced by a criterion such as $\|\mathbf{u}^{(k)} - \mathbf{u}^{(k-1)}\|_2 < \varepsilon_0$ where ε_0 is a small number; m_{\max} is the maximum number of inner split-Bregman iterations, and we find that $m_{\max} = 2$ suffices to produce an accurate result for the second minimization problem in various FWI problems. The computation time of the second minimization problem is trivially small compared to the entire FWI inversion process.

List of Figures

1	A checkerboard model for FWI tests. (a) The true P-wave velocity model and (b) the initial P-wave velocity model for FWI. The black stars in (b) represent 24 randomly-distributed sources, while the blue triangles denote 356 receivers.	29
2	Inverted checkerboard velocity models after 150 iterations using (a) Tikhonov-FWI (b) TV-FWI and (c) TGPV-FWI.	30
3	Velocity profiles at $X = 500$ m selected for the quantitative comparison among the true, the initial and the inverted model using (a) Tikhonov-FWI (b) TV-FWI and (c) TGPV-FWI.	31
4	(a) Relative data misfit and (b) relative model misfit over a total of 150 iterations for the Tikhonov-FWI (black), TV-FWI (blue) and the TGPV-FWI (red).	32
5	(a) A selected slice from the 3D overthrust P-wave velocity model, (b) the spatially varying V_p/V_s ratio, and (c) the resulting S-wave velocity model.	33
6	The initial P-wave (a) and S-wave (b) velocity models for FWI.	34
7	Region of interest selected from the models shown in Fig. 5 for comparison of inversion results. (a) The P-wave velocity and (b) the S-wave velocity.	35
8	Inverted velocity models using (a) Tikhonov-FWI (b) TV-FWI and (c) TGPV-FWI. Panels in (a), (c) and (e) are inverted P-wave velocities and those in (b), (d) and (f) are inverted S-wave velocities.	36
9	Zoom-in views of the region of interest of inverted velocity models in Fig. 8 obtained using (a) Tikhonov-FWI (b) TV-FWI and (c) TGPV-FWI. Panels in (a), (c) and (e) are inverted P-wave velocities and those in (b), (d) and (f) are inverted S-wave velocities.	37
10	Inverted velocity models using (a) Tikhonov-FWI (b) TV-FWI and (c) TGPV-FWI. Panels in (a), (c) and (e) are inverted P-wave velocities and those (b), (d) and (f) are inverted S-wave velocities. All three inversions use sparse seismic data acquired with inadequate numbers of sources and receivers.	38
11	Zoom-in view of the inverted velocity models shown in Fig. 10 using (a) Tikhonov-FWI (b) TV-FWI and (c) TGPV-FWI. (a), (c) and (e) are inverted P-wave velocities and (b), (d) and (f) are inverted S-wave velocities.	39
12	Noise-free (a) and noisy (b) vertical component data of the 40th common-shot gather for the modified elastic SEG/EAGE overthrust model.	40
13	Inverted velocity models produced using (a) Tikhonov-FWI (b) TV-FWI and (c) TGPV-FWI. Panels in (a), (c) and (e) are inverted P-wave velocities and those in (b), (d) and (f) are inverted S-wave velocities. All three inversions use noisy data.	41
14	Zoom-in views of the region of interest in the inverted velocity models shown in Fig. 13 yielded using (a) Tikhonov-FWI (b) TV-FWI and (c) TGPV-FWI. Panels in (a), (c) and (e) are inverted P-wave velocities and those in (b), (d) and (f) are inverted S-wave velocities.	42
15	Inverted velocity models obtained using (a) Tikhonov-FWI (b) TV-FWI and (c) TGPV-FWI. Panels in (a), (c) and (e) are inverted P-wave velocities and those in (b), (d) and (f) are inverted S-wave velocities. All three inversions use dynamic random source encoding.	43

16	Zoom-in views of the region of interest in the inverted velocity models shown in Fig. 15 produced using (a) Tikhonov-FWI (b) TV-FWI and (c) TGPV-FWI. Panels in (a), (c) and (e) are inverted P-wave velocities and those in (b), (d) and (f) are inverted S-wave velocities.	44
17	Data misfits of Tikhonov-FWI, TV-FWI and TGPV-FWI for (a) the first numerical test using all data and for (b) the second numerical test using sparse data. Panels in (c) and (d) show the P- and S-wave velocity model misfits in the second numerical test using sparse data. Panels in (e) and (f) depict the P- and S-wave velocity model misfits in the fourth numerical test using source-encoding inversions.	45
18	The P-wave migration velocity model (a) used as the initial model for FWI of surface seismic data acquired at the Soda Lake geothermal field, together with inversion results obtained using (a) Tikhonov-FWI, (b) TV-FWI, and (c) TGPV-FWI. All three inversions terminate after 100 iterations.	46
19	Comparison of the convergence curves of data misfits for Tikhonov-FWI, TV-FWI and TGPV-FWI of surface seismic data from the Soda Lake geothermal field. . . .	47

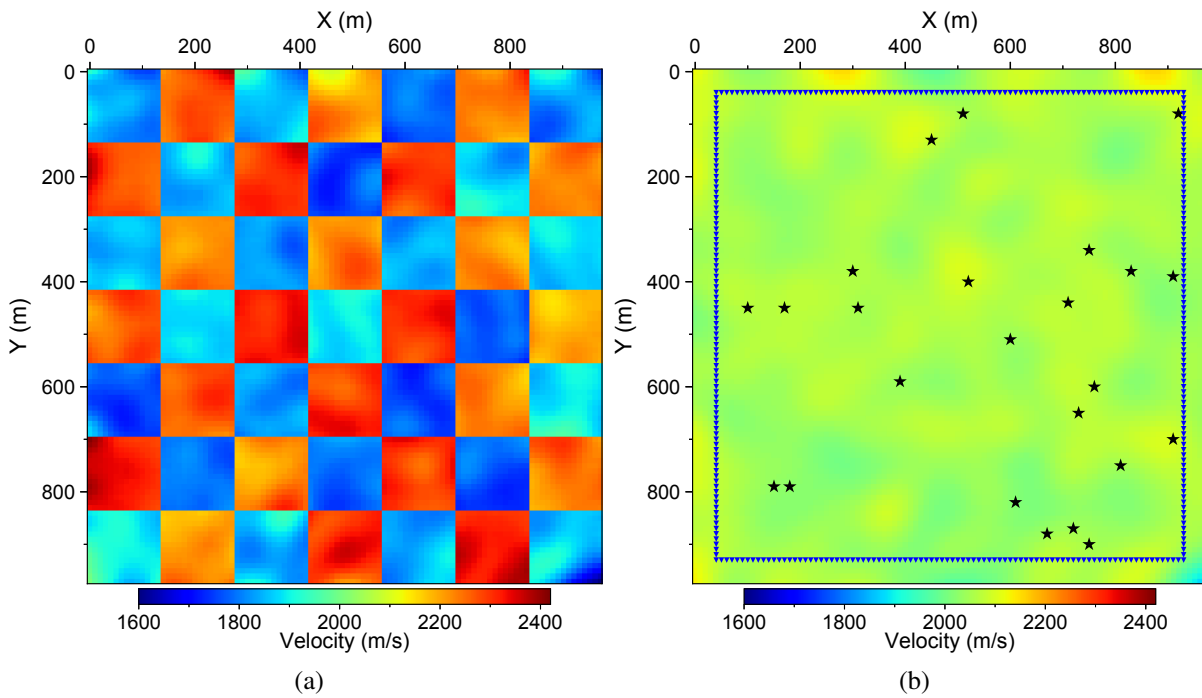


Figure 1: A checkerboard model for FWI tests. (a) The true P-wave velocity model and (b) the initial P-wave velocity model for FWI. The black stars in (b) represent 24 randomly-distributed sources, while the blue triangles denote 356 receivers.

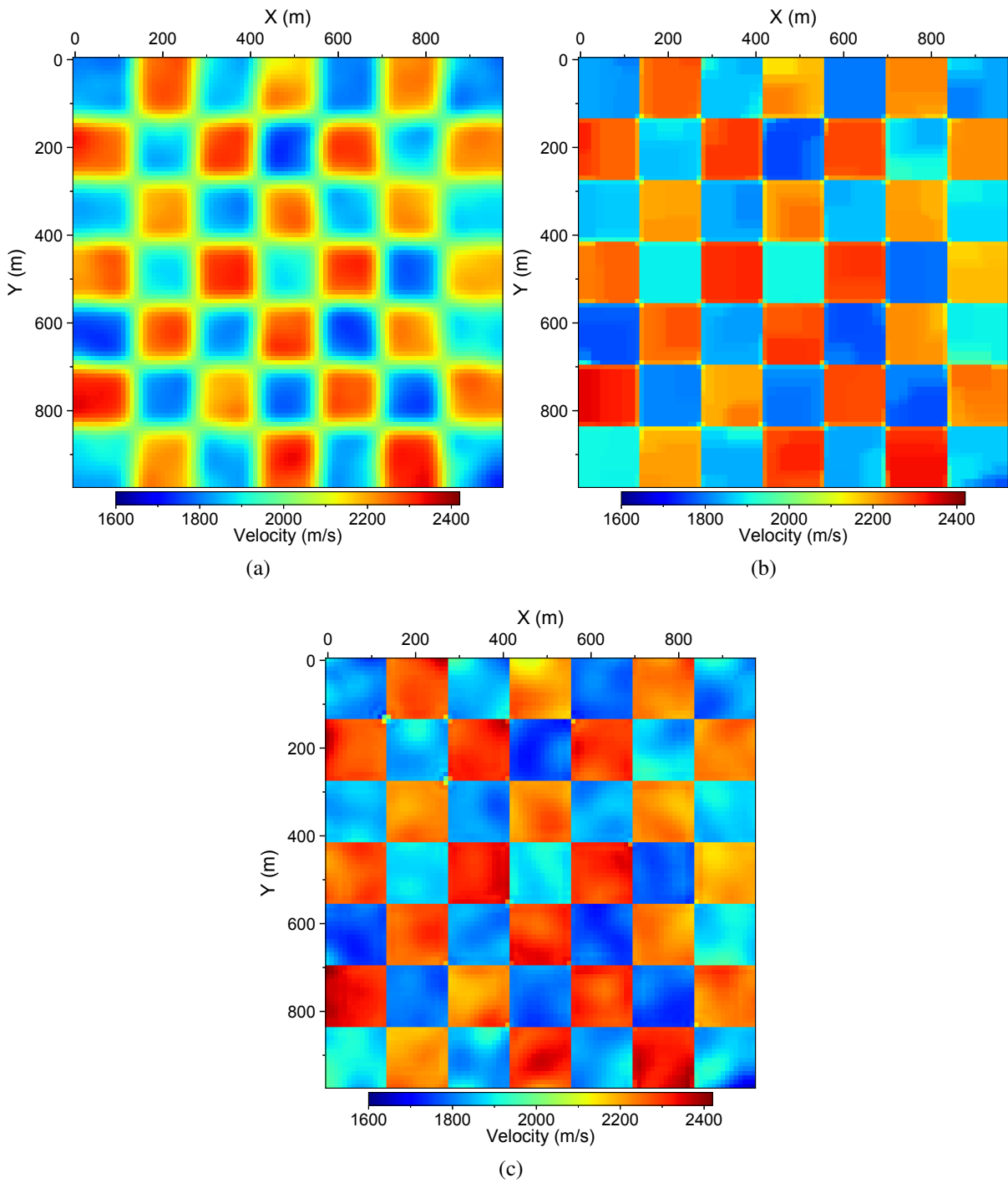


Figure 2: Inverted checkerboard velocity models after 150 iterations using (a) Tikhonov-FWI (b) TV-FWI and (c) TGPV-FWI.

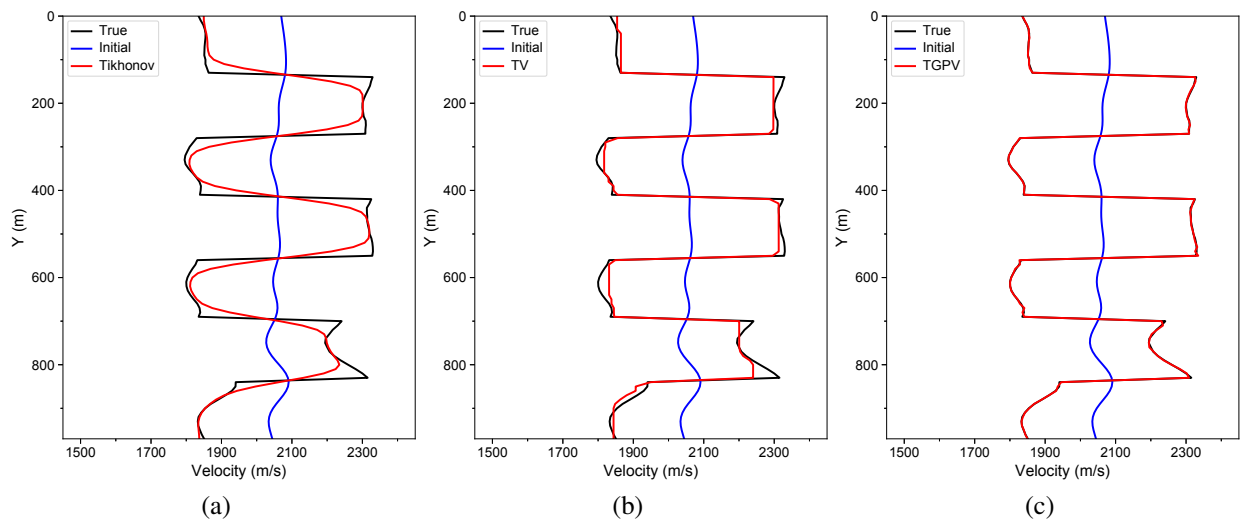
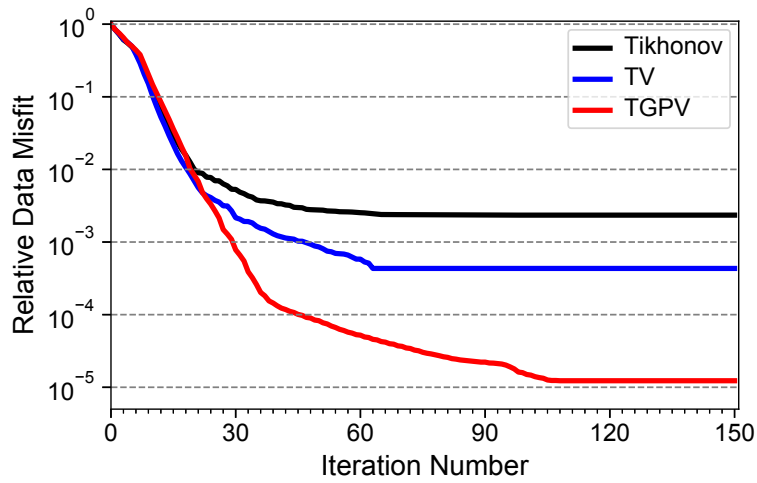
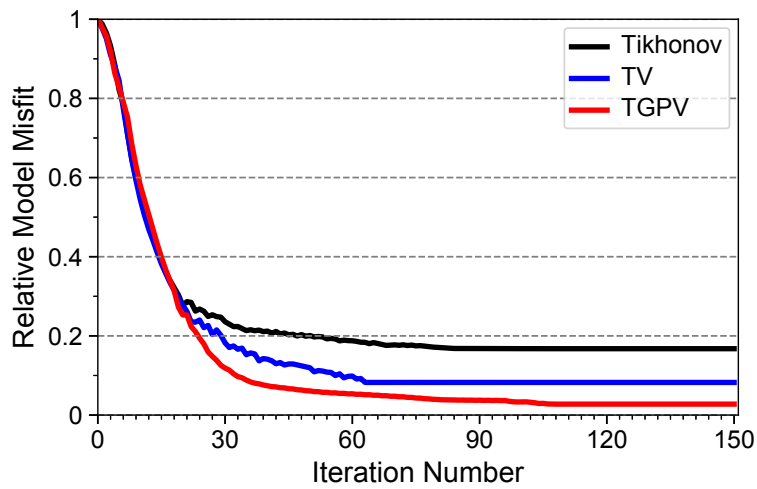


Figure 3: Velocity profiles at $X = 500$ m selected for the quantitative comparison among the true, the initial and the inverted model using (a) Tikhonov-FWI (b) TV-FWI and (c) TGPV-FWI.



(a)



(b)

Figure 4: (a) Relative data misfit and (b) relative model misfit over a total of 150 iterations for the Tikhonov-FWI (black), TV-FWI (blue) and the TGPV-FWI (red).

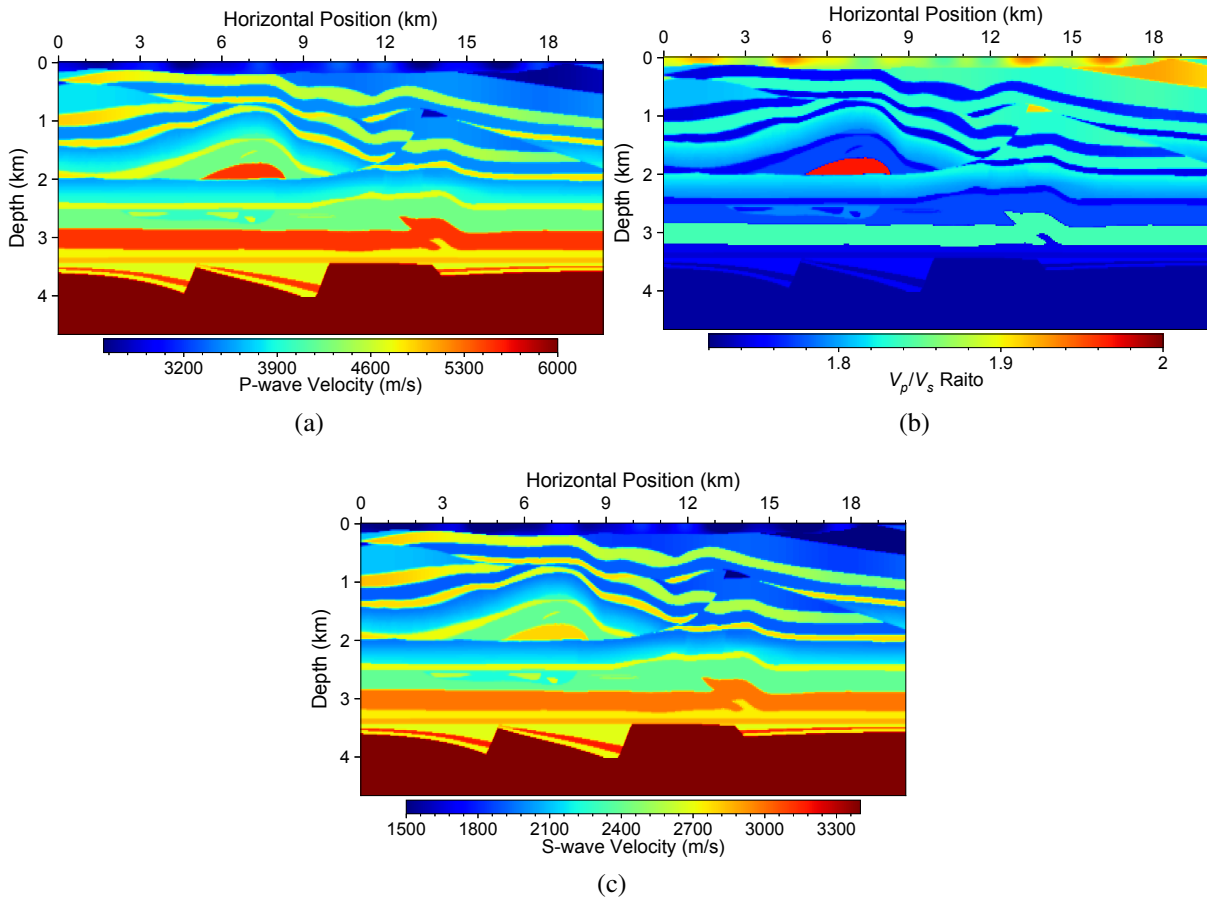


Figure 5: (a) A selected slice from the 3D overthrust P-wave velocity model, (b) the spatially varying V_p/V_s ratio, and (c) the resulting S-wave velocity model.

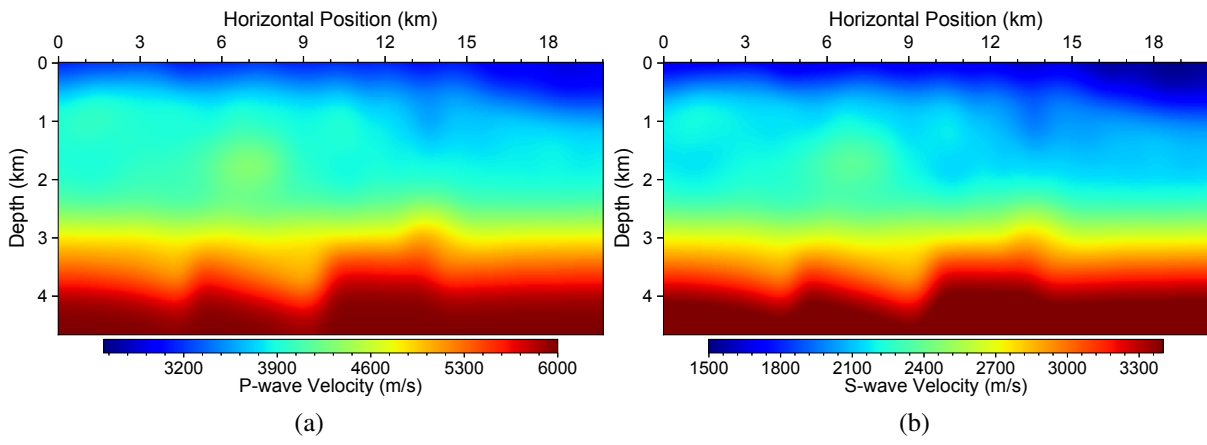


Figure 6: The initial P-wave (a) and S-wave (b) velocity models for FWI.

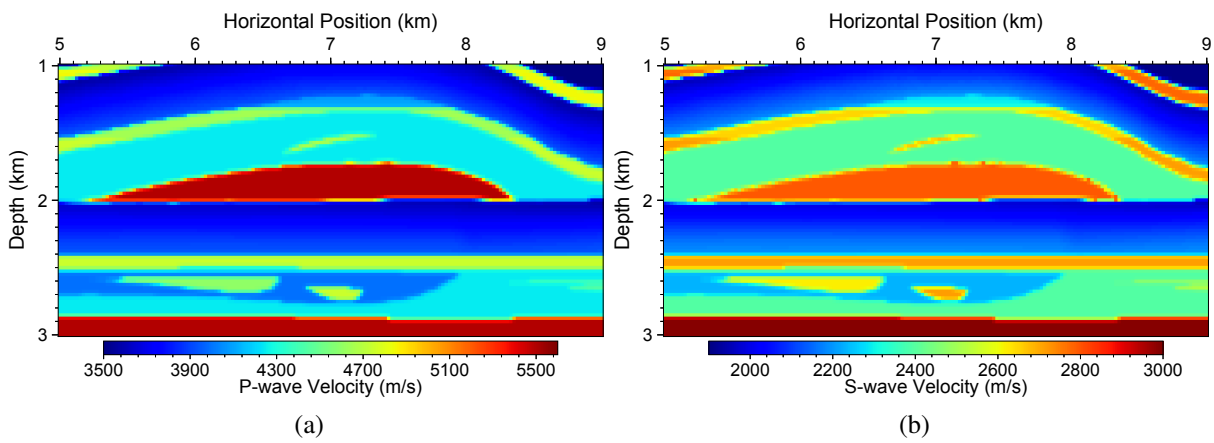


Figure 7: Region of interest selected from the models shown in Fig. 5 for comparison of inversion results. (a) The P-wave velocity and (b) the S-wave velocity.

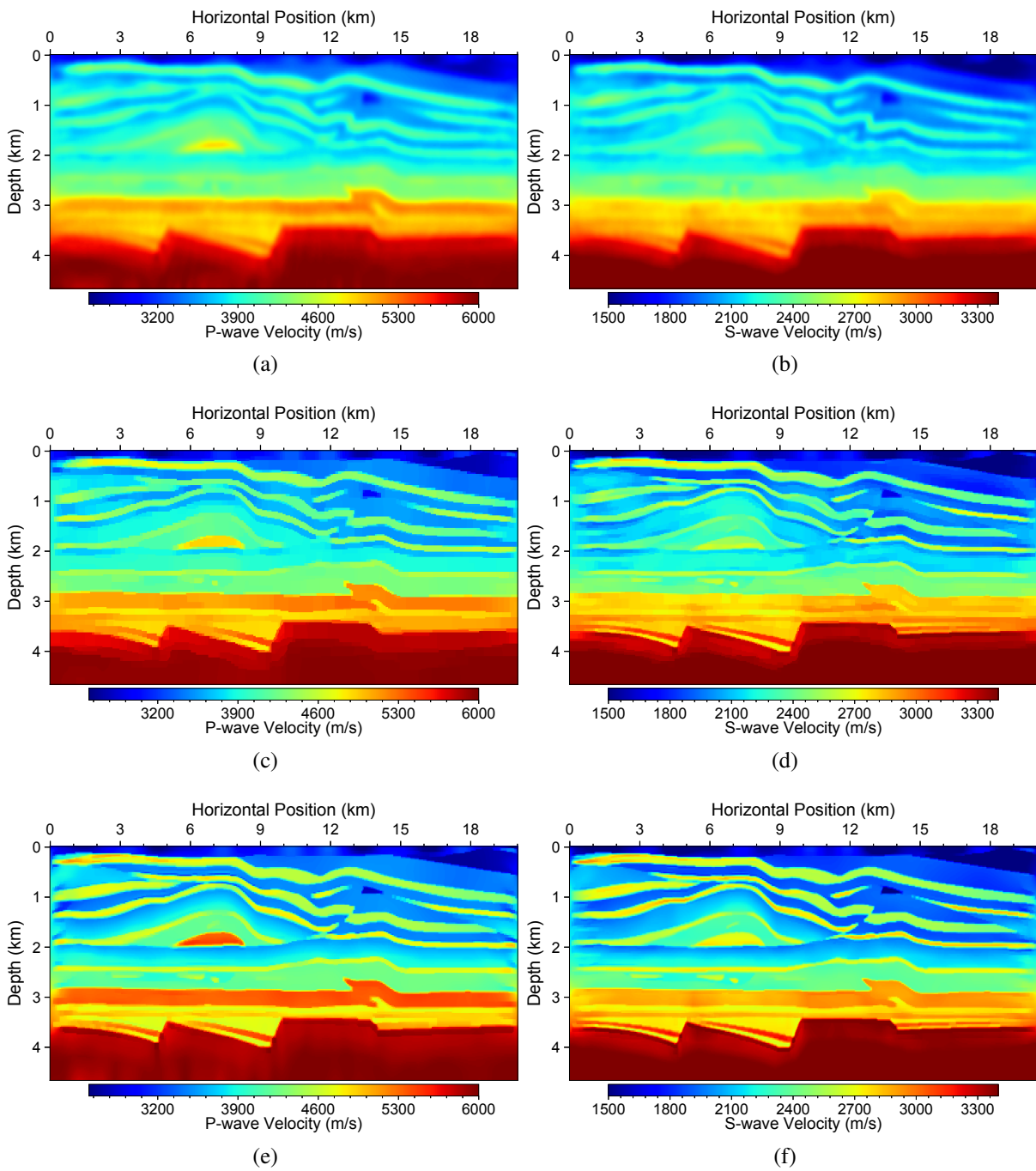


Figure 8: Inverted velocity models using (a) Tikhonov-FWI (b) TV-FWI and (c) TGPV-FWI. Panels in (a), (c) and (e) are inverted P-wave velocities and those in (b), (d) and (f) are inverted S-wave velocities.

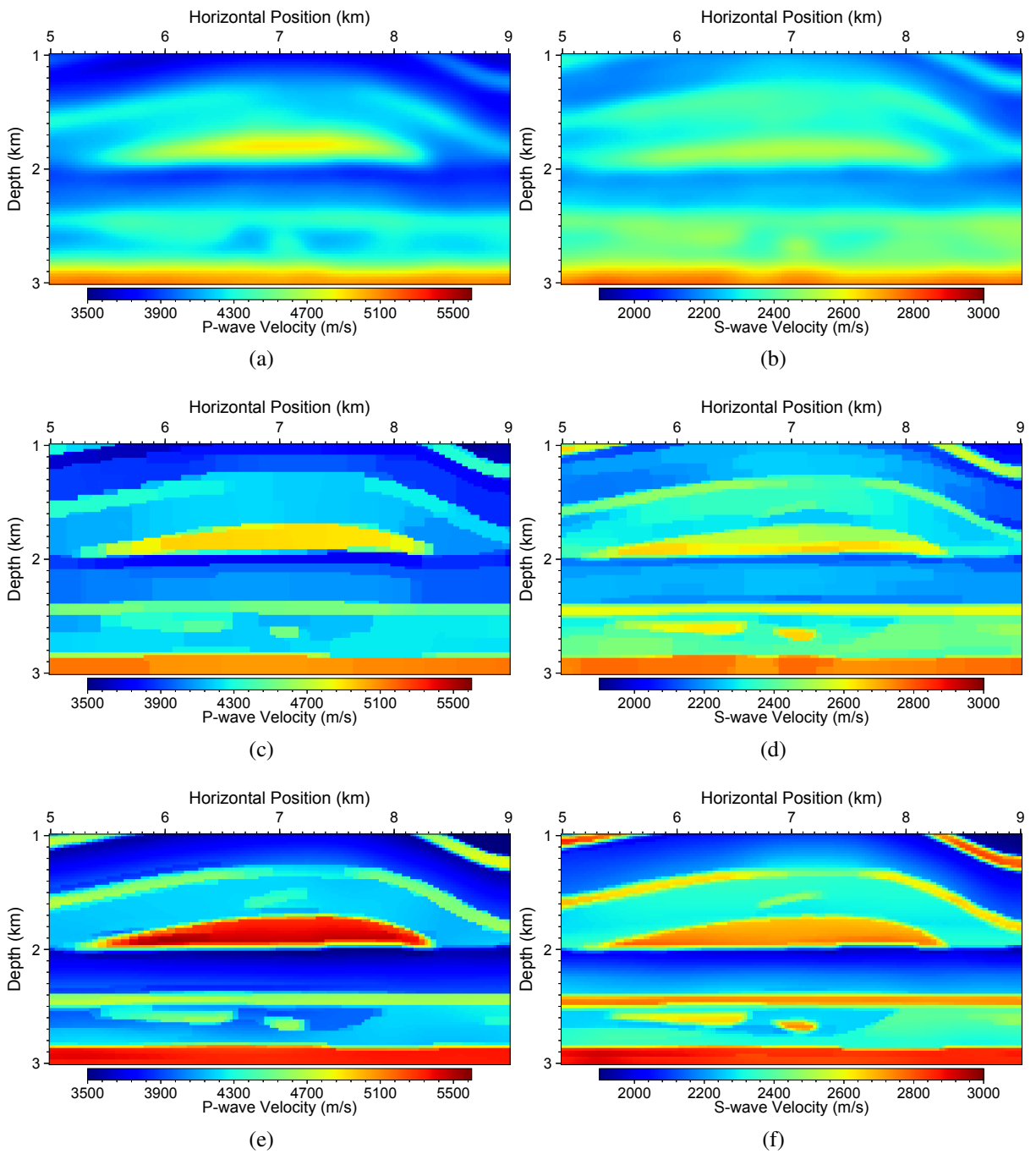


Figure 9: Zoom-in views of the region of interest of inverted velocity models in Fig. 8 obtained using (a) Tikhonov-FWI (b) TV-FWI and (c) TGPV-FWI. Panels in (a), (c) and (e) are inverted P-wave velocities and those in (b), (d) and (f) are inverted S-wave velocities.

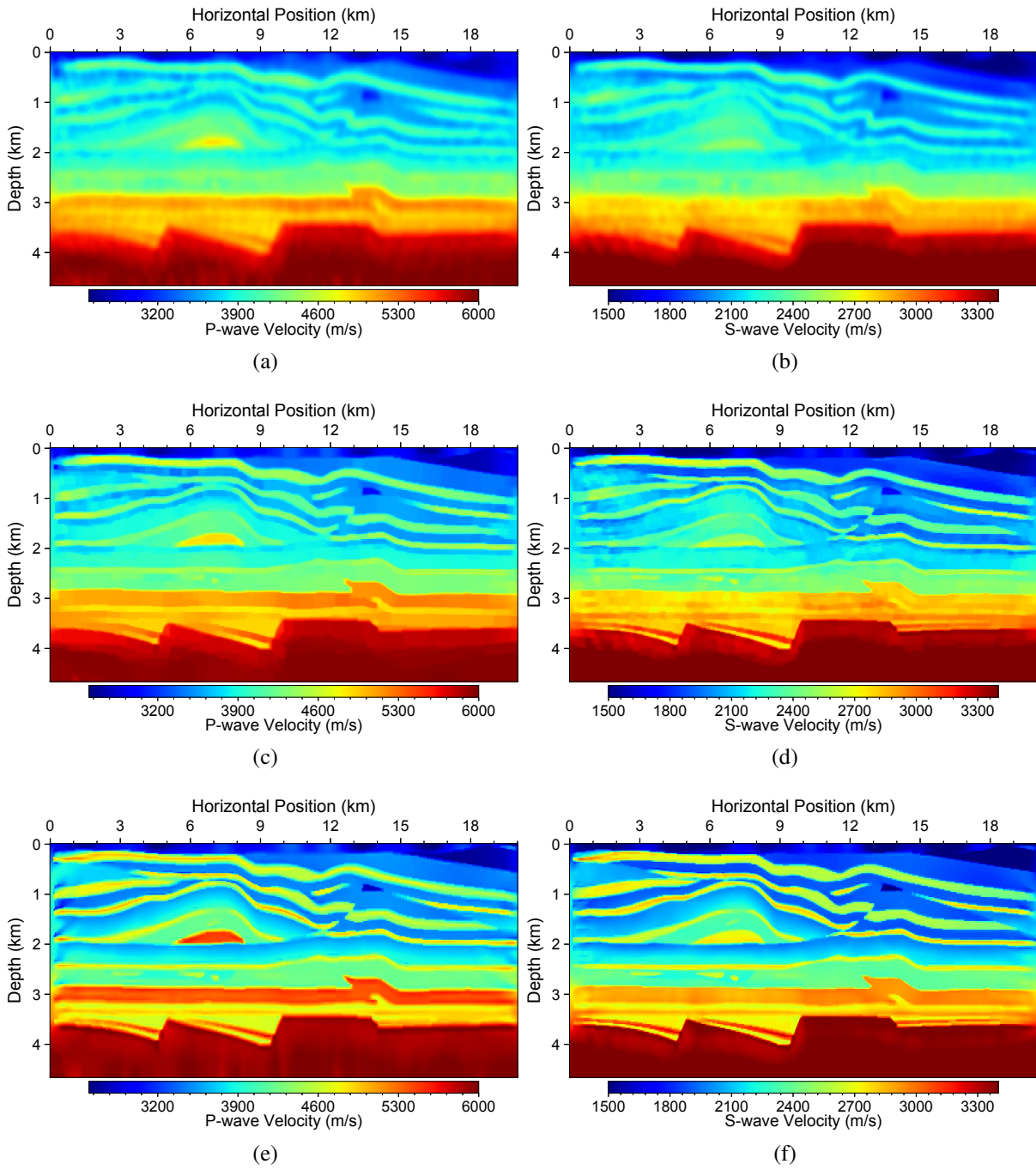


Figure 10: Inverted velocity models using (a) Tikhonov-FWI (b) TV-FWI and (c) TGPV-FWI. Panels in (a), (c) and (e) are inverted P-wave velocities and those (b), (d) and (f) are inverted S-wave velocities. All three inversions use sparse seismic data acquired with inadequate numbers of sources and receivers.

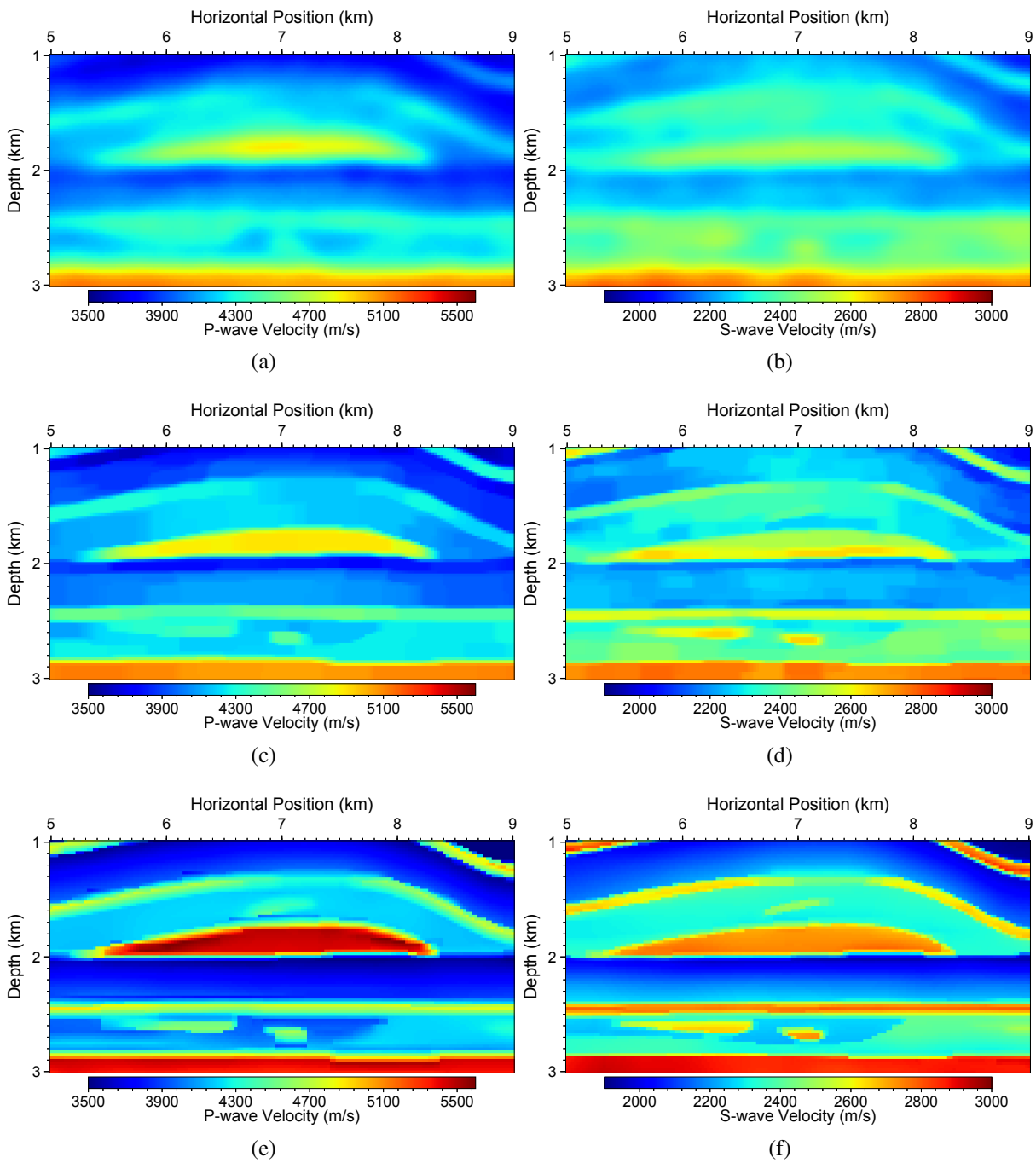


Figure 11: Zoom-in view of the inverted velocity models shown in Fig. 10 using (a) Tikhonov-FWI (b) TV-FWI and (c) TGPV-FWI. (a), (c) and (e) are inverted P-wave velocities and (b), (d) and (f) are inverted S-wave velocities.

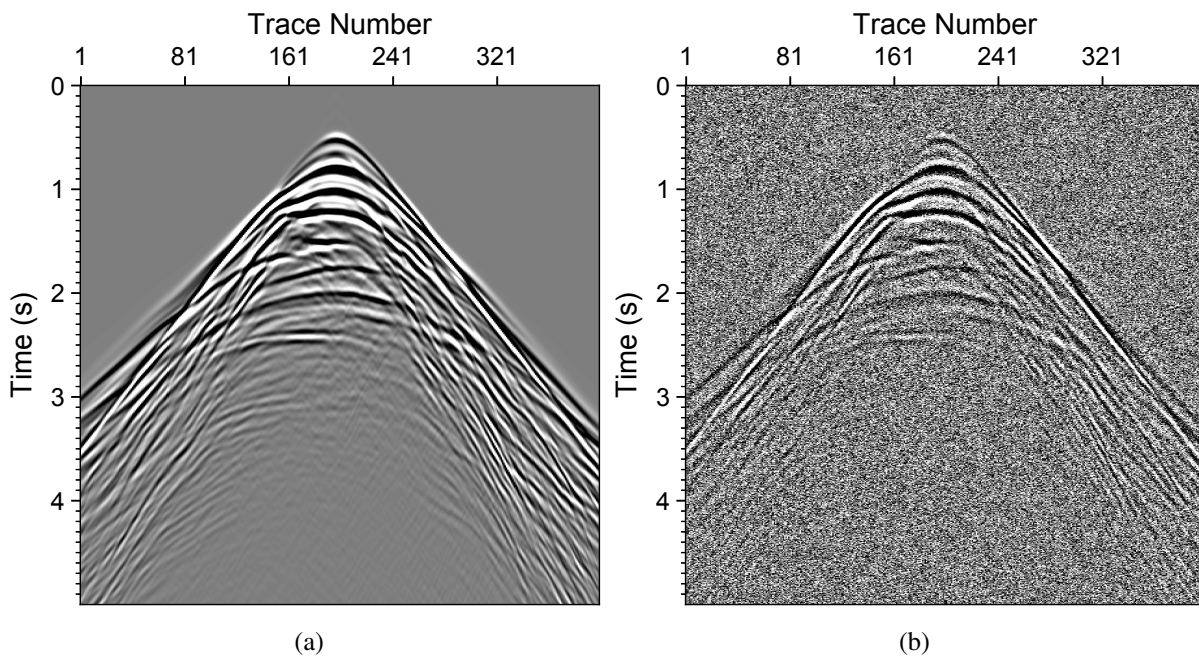


Figure 12: Noise-free (a) and noisy (b) vertical component data of the 40th common-shot gather for the modified elastic SEG/EAGE overthrust model.

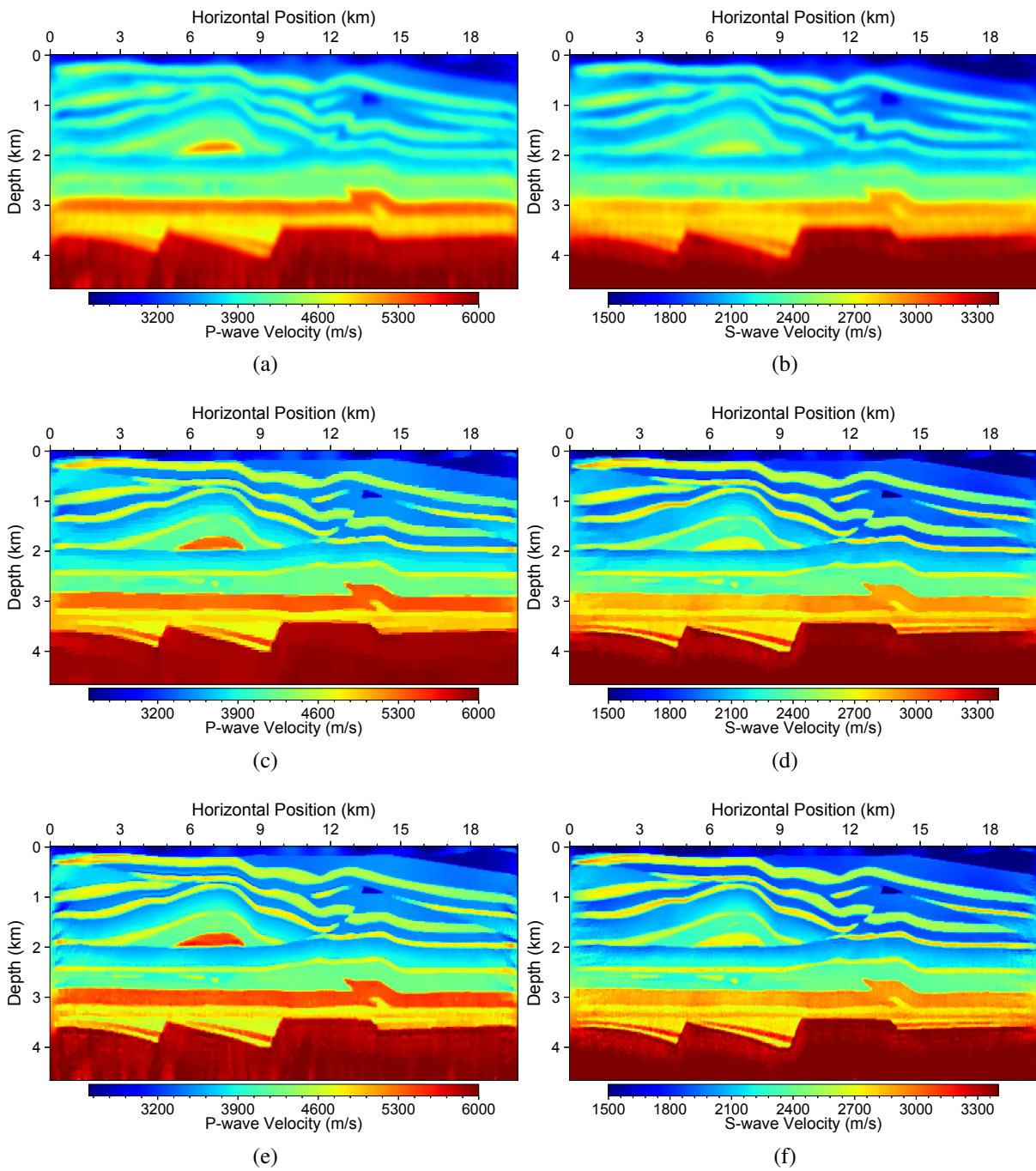


Figure 13: Inverted velocity models produced using (a) Tikhonov-FWI (b) TV-FWI and (c) TGPV-FWI. Panels in (a), (c) and (e) are inverted P-wave velocities and those in (b), (d) and (f) are inverted S-wave velocities. All three inversions use noisy data.

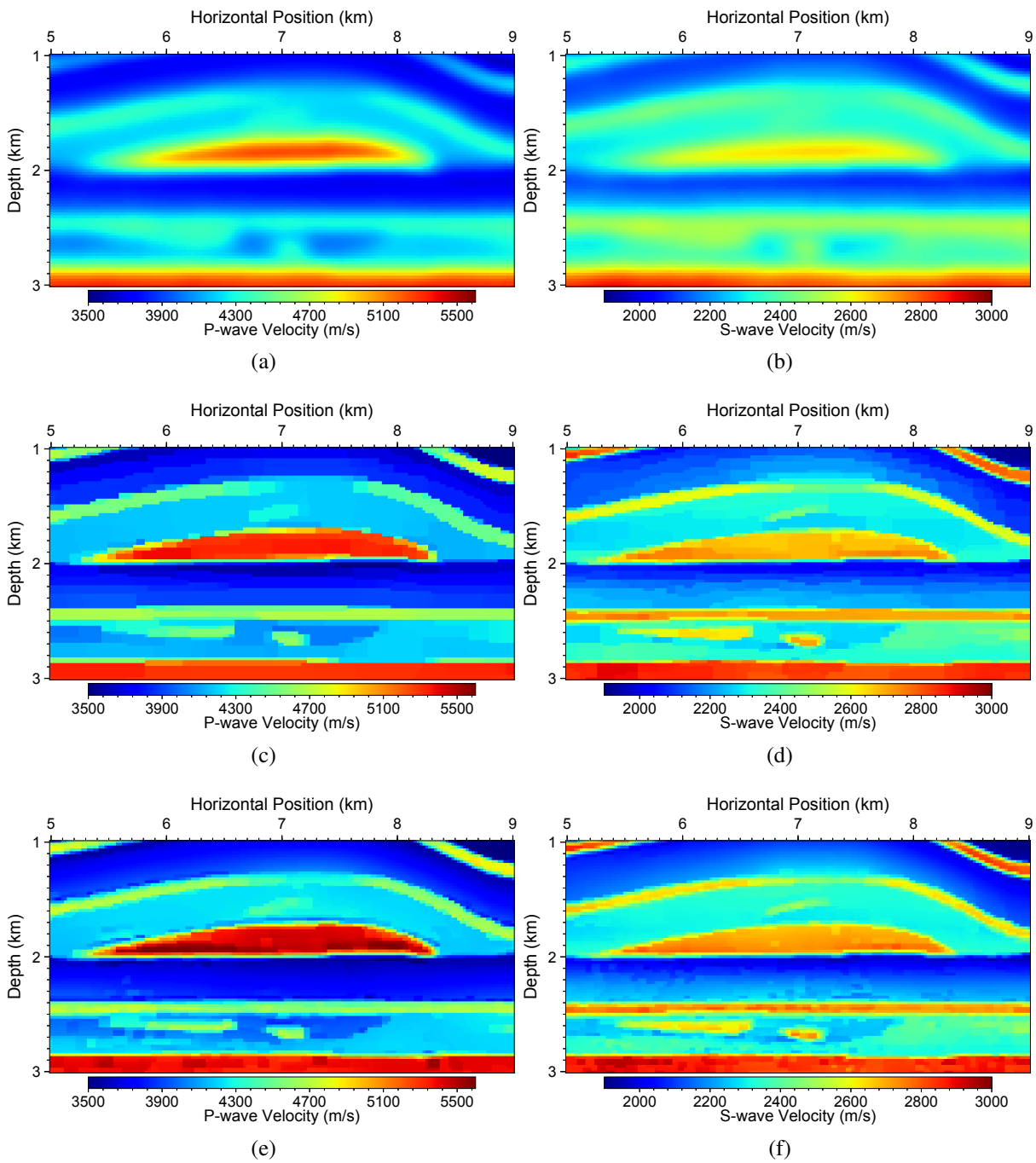


Figure 14: Zoom-in views of the region of interest in the inverted velocity models shown in Fig. 13 yielded using (a) Tikhonov-FWI (b) TV-FWI and (c) TGPV-FWI. Panels in (a), (c) and (e) are inverted P-wave velocities and those in (b), (d) and (f) are inverted S-wave velocities.

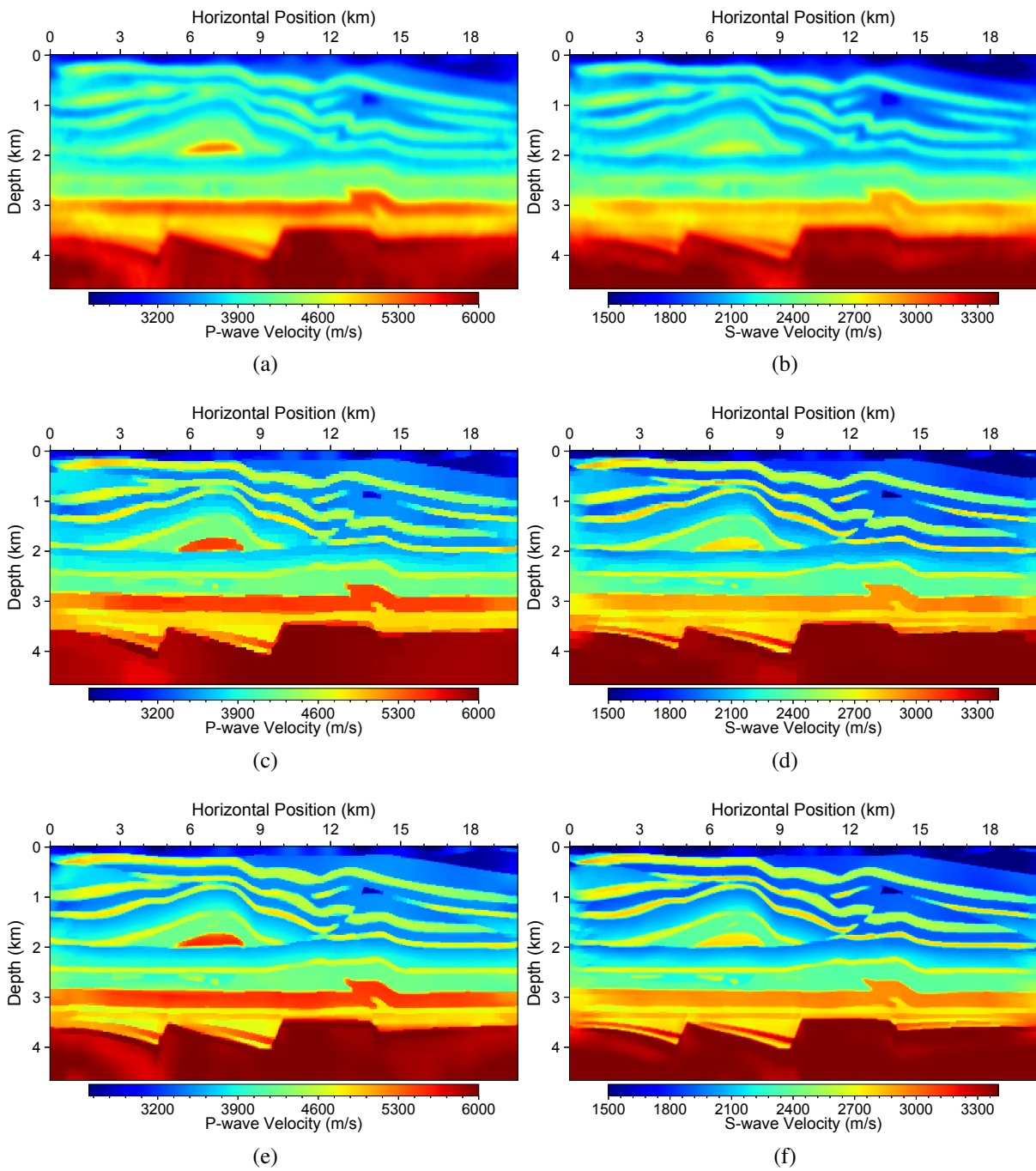


Figure 15: Inverted velocity models obtained using (a) Tikhonov-FWI (b) TV-FWI and (c) TGPV-FWI. Panels in (a), (c) and (e) are inverted P-wave velocities and those in (b), (d) and (f) are inverted S-wave velocities. All three inversions use dynamic random source encoding.

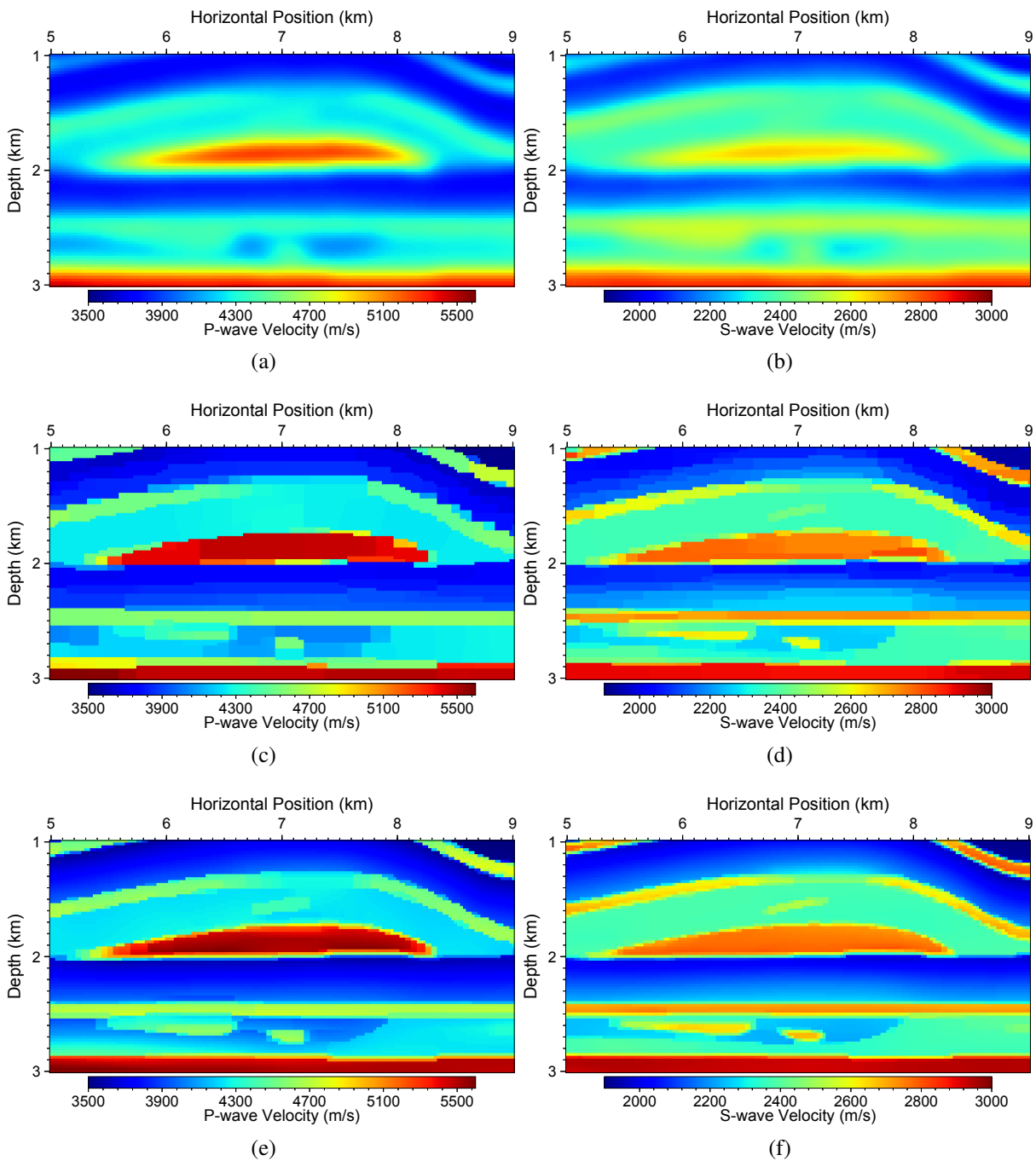


Figure 16: Zoom-in views of the region of interest in the inverted velocity models shown in Fig. 15 produced using (a) Tikhonov-FWI (b) TV-FWI and (c) TGPV-FWI. Panels in (a), (c) and (e) are inverted P-wave velocities and those in (b), (d) and (f) are inverted S-wave velocities.

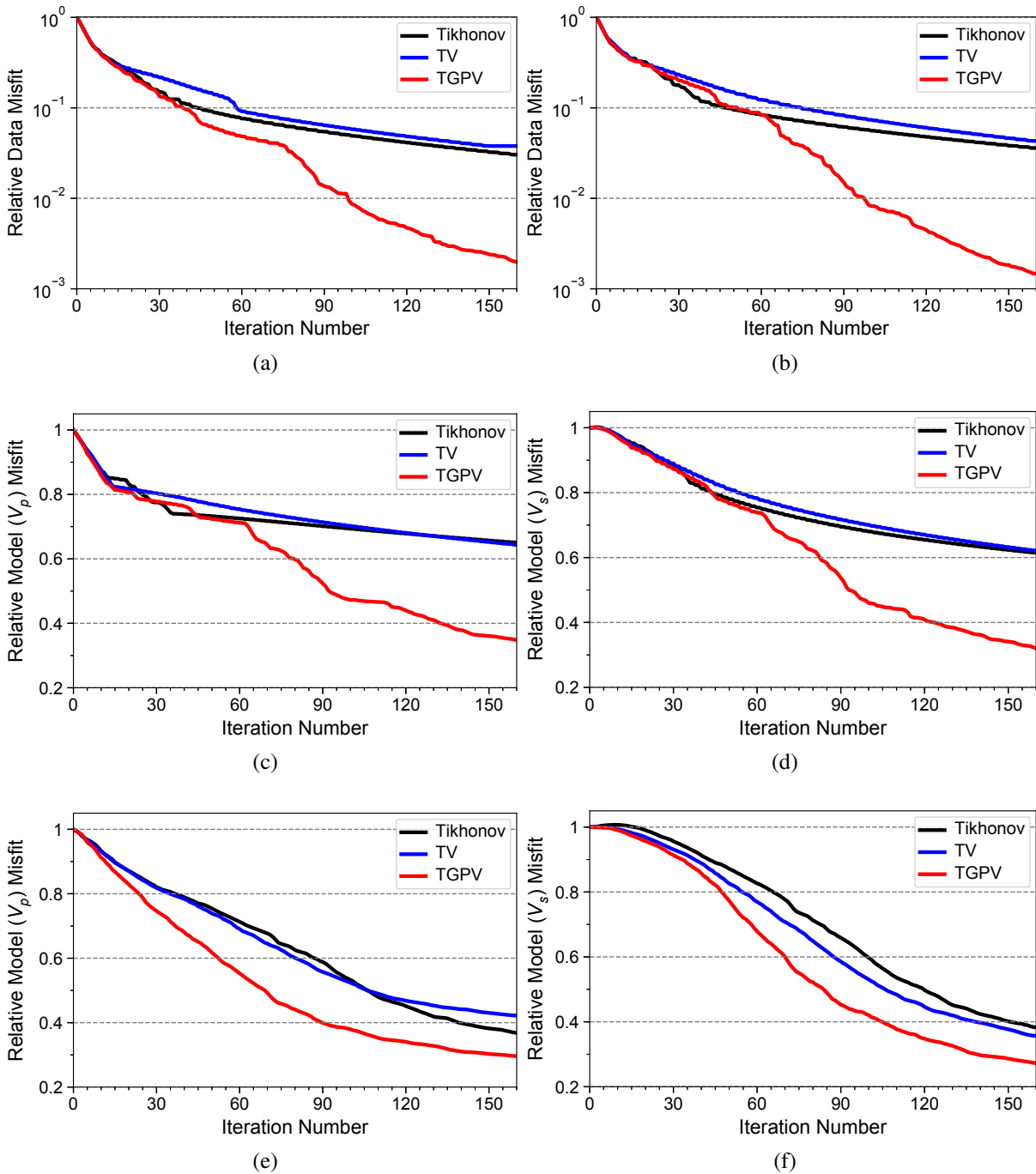
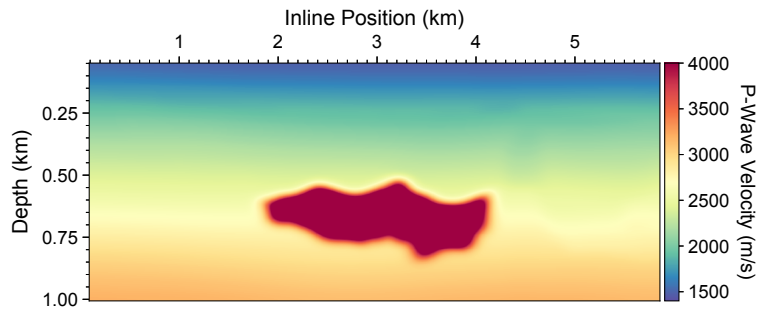
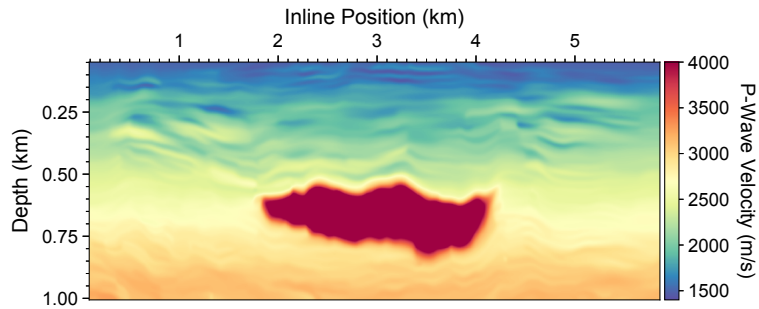


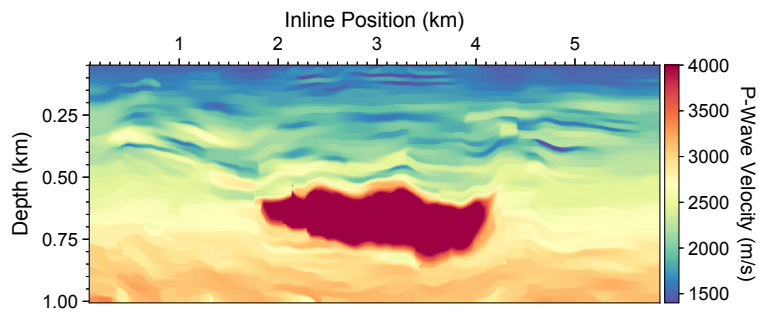
Figure 17: Data misfits of Tikhonov-FWI, TV-FWI and TGPV-FWI for (a) the first numerical test using all data and for (b) the second numerical test using sparse data. Panels in (c) and (d) show the P- and S-wave velocity model misfits in the second numerical test using sparse data. Panels in (e) and (f) depict the P- and S-wave velocity model misfits in the fourth numerical test using source-encoding inversions.



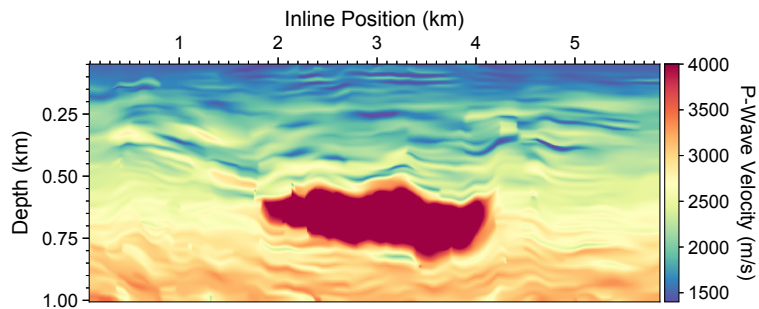
(a)



(b)



(c)



(d)

Figure 18: The P-wave migration velocity model (a) used as the initial model for FWI of surface seismic data acquired at the Soda Lake geothermal field, together with inversion results obtained using (a) Tikhonov-FWI, (b) TV-FWI, and (c) TGPV-FWI. All three inversions terminate after 100 iterations.

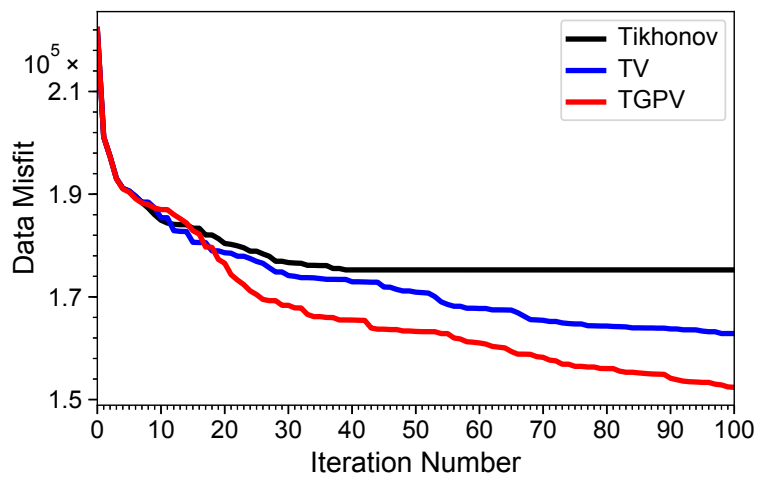


Figure 19: Comparison of the convergence curves of data misfits for Tikhonov-FWI, TV-FWI and TGPV-FWI of surface seismic data from the Soda Lake geothermal field.